Journal: Remote Sensing of Environment

Title: Multi-scale integration of satellite remote sensing improves characterization of dry-season green-up in an Amazon tropical evergreen forest

Author List: Jing Wang[1], Dedi Yang[2], Matteo Detto[3], Bruce W. Nelson[4], Min Chen[5], Kaiyu Guan[6], Shengbiao Wu[1], Zhengbing Yan[1], and Jin Wu[1*]

Author Affiliations:
(1) University of Hong Kong, School of Biological Sciences, Hong Kong, China
(2) Stony Brook University, Ecology and Evolution, Stony Brook, NY, United States
(3) Princeton University, Princeton, NJ, United States
(4) National Institute for Amazon Research (INPA), Manaus, Brazil
(5) Pacific Northwest National Laboratory, Joint Global Change Research Institute, College Park, MD, United States
(6) University of Illinois at Urbana Champaign, College of Agricultural, Consumer and Environmental Sciences, Urbana, IL, United States

*** Corresponding Author:** Jin Wu
School of Biological Sciences, University of Hong Kong, Pokfulam Road, Hong Kong (email: jinwu@hku.hk; phone: +852 2299-0655)

Figures/Tables Record:
Number of figures/tables: 11 figures, 1 table
Supporting materials: 13 figures

Highlights

- A robust method cross-calibrated PlanetScope using BRDF-adjusted MODIS.
- Calibrated data accurately assessed ecosystem-scale and crown-scale reflectance.
- A dry-season decrease in non-photosynthetic vegetation (NPV) fraction was detected.
- Large seasonal trend variability in crown-scale NPV fraction was quantified.

Abstract

In tropical forests, leaf phenology—particularly the pronounced dry-season green-up—strongly regulates biogeochemical cycles of carbon and water fluxes. However, uncertainties remain in the understanding of tropical forest leaf phenology at different spatial scales. Phenocams accurately characterize leaf phenology at the crown and ecosystem scales but are limited to a few sites and time spans of a few years. Time-series satellite observations might fill this gap, but the commonly used satellites (e.g. MODIS, Landsat and Sentinel-2) have resolutions too coarse to characterize single crowns. To resolve this observational challenge, we used the PlanetScope constellation with a 3m resolution and near daily nadir-view coverage. We first developed a rigorous method to cross-calibrate PlanetScope surface reflectance using daily BRDF-adjusted MODIS as the reference. We then used linear spectral unmixing of calibrated PlanetScope to obtain dry-season change in the fractional cover of green vegetation (GV) and non-photosynthetic vegetation (NPV) at the PlanetScope pixel level. We used the Central Amazon Tapajos National Forest k67 site, as all necessary data (from field to phenocam and satellite observations) was available. For this proof of concept, we chose a set of 22 dates of PlanetScope measurements in 2018 and 16 in 2019, all from the six drier months of the year to provide the highest possible cloud-free temporal resolution. Our results show that MODIS-calibrated dry-season PlanetScope data (1) accurately assessed seasonal changes in ecosystem-scale and crown-scale spectral reflectance; (2) detected an increase in ecosystem-scale GV fraction (and a decrease in NPV fraction) from June to November of both years, consistent with local phenocam observations with R^2 around 0.8; and (3) monitored large seasonal trend variability in crown-scale NPV fraction. Our results highlight the potential of integrating multi-scale satellite observations to extend fine-scale leaf phenology monitoring beyond the spatial limits of phenocams.

Keywords: Multi-scale satellite observations, PlanetScope, MODIS, BRDF correction, reflectance cross-calibration, leaf phenology, non-photosynthetic vegetation, individual tree crowns.

1. Introduction

Leaf phenology dominates seasonal and spatial variability in carbon and water fluxes (Jung et al., 2019; Restrepo-Coupe et al., 2013), with important vegetation mediated feedbacks to regional and global climates (Bonan, 2008; Wright et al., 2017). At the ecosystem scale, leaf phenology emerges from all individuals and species living in a plant community, and the phenology of these individuals shows large differential sensitivity response to climate change, even within a temperate deciduous forest community (Richardson et al., 2018). Therefore, it is increasingly important for the field to move towards the study of leaf phenology at the individual tree-crown level.

Compared with the highly predictable phenological cycles in the temperate biomes, leaf phenology in tropical evergreen forests is even more complex and less understood (Albert et al., 2019; Reich, 1995). Much recent evidence from ground observations (Detto et al., 2018; Xu et al., 2017) and phenocams (de Moura et al., 2017; Lopes et al., 2016) shows unusual leaf phenology patterns in tropical "evergreen" forests. That is, the forest ecosystem appears evergreen all year round, but strong seasonal leaf phenology dynamics occur at the tree-crown level with two typical patterns. First, about 60-70% of all individuals rapidly exchange old leaves for new leaves during the high-sunlight dry season (Gonçalves et al., 2020; Wu et al., 2016). Second, also in the dry season, some upper canopy crowns drop part or all of their leaves and remain the leafless status for few weeks prior to massive new leaf flush. These unique phenology patterns further cause strong seasonal variation in ecosystem-scale leaf quality (i.e. photosynthetic capacity and optical properties) as a function of leaf age mix, which helps explain the large dry season increase in tropical forest photosynthesis (Albert et al., 2018; Wu et al., 2016) and satellite-detected greenness (Wu et al., 2018). Despite the increasing importance of crown-scale phenology study in multiple ecology-related fields, there is yet lacking high resolution monitoring that can help interpret fine-scale phenological dynamics and explain large spatial heterogeneity across forest landscapes. Therefore, accurate characterization and understanding of tropical leaf phenology (i.e. particularly the pronounced dry-season phenological variations and green-up) at different spatial scales remain an essential problem in tropical ecology studies.

However, several challenges remain. Phenocams may be the most accurate way to quantify tropical leaf phenology from individual tree-crowns up to landscapes (Alberton et al., 2017; Lopes et al., 2016; Moore et al., 2016), but are very limited in their footprints and time spans. For example,

92 a phenocam mounted on a 60m tower typically covers only dozens of upper canopy tree-crowns
93 within an area of several hectares (Wu et al., 2016). In addition, existing phenocams have been
94 deployed at only a few forest sites and span a few years (e.g. e-phenocam network in Brazil,
95 http://www.recod.ic.unicamp.br/ephenology/client/index.html#/phenocamNetwork). Satellite
96 remote sensing with large area coverage and frequent revisits can be a powerful alternative solution
97 (Huete et al., 2002, 2006). Unfortunately, as shown in a recent ground-based tree survey study in
98 an Amazon evergreen forest of French Guiana (Blanchard et al., 2016), the crown diameter for
99 tropical canopy crowns is normally small, ranging from a few meters to tens of meters at most. As
100 such, most commonly used satellite observations, such as Moderate Resolution Imaging
101 Spectroradiometer (MODIS) of 500m per pixel, Landsat of 30m, and Sentinel-2 of 10m, remain
102 too coarse to monitor leaf phenology dynamics at the individual tree-crown scale.
103 The increasing availability of high spatial and temporal resolution satellite data offers an
104 unprecedented opportunity to help resolve both the spatial coverage limitation of phenocams and
105 the lack of tree-crown scale observations from coarse-resolution satellite remote sensing.
106 Particularly, the PlanetScope constellation of more than 120 sensors (Planet Labs Inc., San
107 Francisco, CA) has several advantages, including daily-to-weekly global coverage at a 3m spatial
108 resolution and near-nadir view (Planet Team, 2018), but has not yet been fully explored. As with
109 other optical orbital sensors (e.g. Galvao et al., 2011; Samanta et al., 2010), the PlanetScope
110 reflectance products are also subject to cloud/aerosol contamination and the Bidirectional
111 Reflectance Distribution Function (BRDF) effect that is associated with image acquisition under
112 variable illumination and sensor viewing geometries. Individual PlanetScope sensors also have
113 inconsistencies in their DN scaling (Houborg and McCabe, 2018a, 2018b). However, a rigorous
114 method to utilize PlanetScope data to aid assessments of land surface reflectance seasonality is
115 neither developed yet nor rigorously evaluated. Additionally, multiple biophysical processes, such
116 as seasonal variations in canopy leaf area index (LAI), in leaf age mix and in canopy structure, can
117 affect canopy reflectance seasonality simultaneously (Wu et al., 2018), making it difficult to
118 directly connect observed canopy reflectance seasonality with leaf phenology (e.g. leafy versus
119 leafless phenostages) at the tree-crown scale.
120 Recent advances in satellite data fusion techniques and improved biophysical
121 understanding of satellite reflectance products appear to be promising for application of fine-scale
122 phenology monitoring in tropical evergreen forests. For example, by first calibrating Landsat using

BRDF-adjusted MODIS data and then explicitly accounting for both spatial (from 30m spatial resolution Landsat) and temporal (from daily MODIS) variations, Luo et al. (2018) demonstrated the feasibility to combine MODIS and Landsat satellites to enable land surface monitoring at daily, 30m resolution. This suggests the technical feasibility to integrate MODIS and PlanetScope data to enable high-resolution phenology monitoring at a 3m resolution in tropical evergreen forests. Additionally, several recent studies demonstrate the feasibility to differentiate leafless tree-crowns from leafy tree-crowns using high-resolution satellite images, such as QuickBird of a 2.62m resolution (Lopes et al., 2016) and WorldView-2 of a 1.84m resolution (Wu et al., 2018). The underlying biophysical basis is that the reflectance spectra of leafless tree-crowns are significantly different from those of leafy tree-crowns—a phenomenon that has been commonly observed across multiple tropical forest sites over large tropical areas (Clark and Roberts, 2012; Lopes et al., 2016; Viennois et al., 2013; Wu et al., 2018). As such, we believe high-resolution satellite data like PlanetScope could offer a novel means to quantitatively differentiate the green vegetation (GV) fraction from that of non-photosynthetic vegetation (NPV) in the upper canopy of tropical evergreen forests.

The goal of this study is to investigate the technical feasibility and mechanistic soundness of integrating MODIS and PlanetScope data for cross-scale (from fine-scale of 3m to landscapes of a few kilometers) phenology monitoring, with a particular focus on the dry-season phenological trend. Specifically, we first developed a method to rigorously cross-calibrate PlanetScope reflectance data using BRDF-adjusted MODIS. We then evaluated the fine-scale robustness of the developed method by assessing the seasonal reflectance pattern of permanent objects and assessed the large-scale robustness by comparing ecosystem-scale seasonal reflectance pattern of the calibrated data with the corresponding pattern from MODIS. Further, we estimated fractions of GV and NPV at the pixel and ecosystem levels, using a linear spectral unmixing model. By this means, we hope to use a metric of NPV fraction (or GV fraction) with clear biophysical meaning for tropical phenology monitoring. For this proof-of-concept, we focus on the Central Amazon dry season, when crown-scale and ecosystem-scale leaf phenology changes are more pronounced and when more frequent cloud-free images are available.

2. Study site and materials

2.1 Study site

A Central Amazon tropical evergreen forest at the k67 eddy covariance tower site (54°58'W, 2°51'S) was used in this study (Fig. 1a). It is the Tapajos National Forest, near Santarém, Pará, Brazil. We selected this site for three reasons. First, there were rich related field observations previously made at this forest site, including both field and tower-phenocam measurements of leaf phenology (Brando et al., 2010; Wu et al., 2016). Second, the forest is on an extensive well-drained clay-soil plateau (Rice et al., 2004), which minimizes the effects of topography on satellite-detected canopy reflectance (Matsushita et al., 2007) and thus makes it easy to interpret satellite data. Third, it is a typical tropical evergreen forest in the Central Amazon, and ground-observed phenology pattern in this site is very comparable with that of other Central Amazon tropical forests near Manaus, Brazil (Lopes et al., 2016; Wu et al 2016). Additionally, similar to other tropical evergreen forests (Eamus, 1999), it has rich plant diversity and includes vast variability in crown-level leaf phenology ranging from evergreen to semi deciduous and fully (but briefly) deciduous. The forest has a mean annual air temperature of 26 °C (Hutyra et al., 2007), and a mean annual precipitation of 2022 mm yr^{-1} with a 5-month-long dry season from July to November (Wu et al., 2016). For details about forest composition and structure of the k67 site see Rice et al. (2004). About 37 km north of this forest site is the town of Alter do Chão, which is predominated by the urban land cover type with some mixture of forests as well. The urban area, particularly the building materials with constant reflectance spectra after BRDF correction, was included to evaluate the robustness of our method (see Section 3.2.4).

2.2 Materials

Four different kinds of data were available at k67 to characterize leaf phenology patterns. These include field measurements of LAI, tower-phenocam measurements of tree-crown phenostages (i.e. leafy versus leafless), and two types of optical satellite remote sensing (PlanetScope and MODIS). Since different datasets were sampled in different time periods with various durations while optical satellites were subject to heavy cloud contamination in the wet season, to minimize all these effects, we limited our study to trends in the long dry season. Specifically, we aimed to use field- and tower-based phenology measurements to help evaluate satellite-derived phenology metrics.

Field measurements of LAI (projected leaf area per unit ground area, m^2m^{-2}) were previously made monthly from January 2000 to December 2005 at 100 grid points systematically

distributed in a 1-ha plot, ~5km from the k67 tower site, using two LiCor-2000 Plant Canopy Analyzers (LiCOR Inc., Lincoln, NE). For details regarding the data and data collection procedure see Brando et al. (2010). We here used the mean annual cycle of monthly field-observed LAI to indicate the average ecosystem-scale phenology pattern of this forest site.

A 3-band (NIR, red, and green) Tetracam Agricultural Digital Camera (Tetracam Inc., Chatsworth, CA) was mounted on the k67 eddy covariance tower for leaf phenology monitoring (Fig. 1b). It had a field of view of about 200×300 m^2, covering around 65 upper canopy tree crowns. The phenocam was programmed for automatic image acquisition at a 30-minute interval from January 2010 to December 2011. The image acquisition stopped afterwards. For more details on the phenocam data as well as the method used for phenology analysis, see Wu et al. (2016). Below we briefly summarized the visual assessment approach (or 'crown-based phenology inventory' shown in Wu et al., 2016) for phenology analysis at k67. The approach includes the following five steps: i) we manually selected a best quality image every 6 days (i.e. overcast, near local noon, and free from shadows/rain/fog) throughout the entire image time series; ii) we divided the image of forest landscape into discrete regions of interest (ROIs) that corresponded to each individual well-illuminated tree-crown; iii) for each selected image we surveyed all the identified tree-crowns, and visually assigned each crown to one of two phenostages: leafless (leaf shedding or bare branch materials accounts for around or more than 50% of the entire tree crown area) or leafy (otherwise), based on their colors, textures and temporal trends of leaf color within the adjacent two weeks; iv) for each selected image, we calculated a metric called 'leafless tree-crowns fraction' (1- 'leafy tree-crowns fraction') by dividing the number of leafless tree-crowns by all identified tree-crowns (n=65), and v) a mean annual cycle of monthly 'leafless tree-crowns fraction' (or NPV fraction) was derived to indicate ecosystem-scale average phenology at k67.

The four-band high-resolution PlanetScope data from Planet Labs Inc. were used (Fig. 1c and Table 1). Planet Labs Inc. is an American private Earth imaging company, which offers daily images of global coverage, including PlanetScope (3m resolution, daily revisit cycle with near nadir view) and RapidEye (5m resolution, 5.5 days revisit cycle with near nadir view) satellite imagery. Researchers can access PlanetScope data through a research and education license. We here used the PlanetScope data, as it has finer spatial and temporal resolutions compared with RapidEye. At k67, we surveyed all available PlanetScope data for 2018 and 2019, and found no good wet season images (January to May, plus December) due to heavy cloud contamination.

Therefore, only the six months (June to November) PlanetScope data with low cloud cover (<40%; predetermined by cloud filter provided by Planet Lab Inc.) were downloaded and used, including 22 dates in 2018 and 16 dates in 2019. For clarity purposes, we focus on the 22 dates of measurements from 2018 in the main text. Results for 2019, which are very similar as the results for 2018, are in supplementary materials. At the Alter do Chão site, a total of 30 dates of PlanetScope measurements in 2018 from June to December were downloaded and used. For all PlanetScope data used in this study, the sensor viewing angle was less than 1.2° off nadir.

The coarse-resolution MODIS data was also used (Fig. 1d). Since MODIS covers the four bands of PlanetScope (Table 1), it makes the integration of these two satellites possible. Here we used the MODIS BRDF/Albedo model parameter product, MCD43A1 (Schaaf et al., 2002), for three reasons. First, increasing evidence suggests that the BRDF effect associated with sun-sensor geometry is an important confounding factor affecting satellite-detected phenology in tropical forests (Galvao et al., 2011; Morton et al., 2014; Saleska et al., 2016). Second, BRDF-adjusted MODIS products detect tropical forest phenology in good agreement with ground measurements (Lopes et al., 2016; Wagner et al., 2016). Third, the BRDF-adjusted MODIS products from MCD43A1 have been rigorously validated previously (Maeda et al., 2016; Wu et al., 2018). The daily MCD43A1 data of 500m from February of 2000 to December of 2019 were downloaded. We then computed the BRDF-adjusted reflectance at a simulated nadir view, 0° relative azimuth angle, and 45° solar zenith angle, using the BRDF model parameters in the MCD43A1 data as inputs to the semi-empirical RossThick-LiSparse reciprocal model (Wanner et al., 1995).

For the satellite data used in this study, there are four spatial extents involved and each has a distinct purpose. First, we used a 10km×10km area of plateau forest (Fig. 1c, d) representing the entire k67 site for cross-calibration by histogram matching between PlanetScope and MODIS (see Section 3.2.3). This is because a significant amount of pixels after quality control are needed for proper histogram matching, and the 10km×10km area provides sufficient valid MODIS pixels after quality control. One PlanetScope scene often may not cover the whole area, and thus in our study, multiple PlanetScope scenes of the same day were mosaicked and cropped for a full coverage of the 10km×10km area. Second, we used an 8km×8km area for the Alter do Chão site (Fig. 1e, f), and PlanetScope data of this site was firstly used to identify the permanent objects (i.e. buildings) that are spectrally stable and then used to evaluate the robustness of our method (see Section 3.2.4). Third, we used a moving window of a 5km×5km area surrounding a target pixel to firstly generate

the quality assurance (QA) flag (i.e. QA30; more details shown in Section 3.1) for that pixel and then assessed the gap-filling procedure based on its QA time series (more details shown in Section 3.2.2). Fourth, we used a 3km×3km area centered on the k67 tower to calculate the seasonal trends of ecosystem-scale phenology derived from PlanetScope and MODIS, and then compared them with field and phenocam observations of leaf phenology.

3. Methods

In order to develop a rigorous method that integrates high-resolution PlanetScope with coarse-resolution MODIS for cross-scale phenology monitoring in tropical forests, we divided the work into the following four tasks: 1) acquiring and processing PlanetScope and MODIS data; 2) cross-calibrating PlanetScope data using BRDF-adjusted MODIS as the reference; 3) extracting reflectance spectra of the three key endmembers comprising tropical forest canopies (NPV, GV and shade; also see Fig. S1 for these example endmembers shown in a WorldView-2 image at the k67 site), and estimating endmember fractions for each calibrated PlanetScope image using a linear spectral unmixing model; and 4) evaluating the accuracy of derived seasonal trends in NPV and GV fractions from calibrated PlanetScope by comparing with ground and phenocam observations of leaf phenology. The first two tasks aim to improve the data quality of PlanetScope by developing consistent data processing tied to high quality data. The last two tasks aim to improve biophysical interpretation of PlanetScope data, by transforming surface reflectances to fractional covers of the real-world constituents of tropical forest canopy. A flow chart that summarizes the method and the four key tasks is shown in Fig. 2.

3.1 (Task 1): Acquiring and processing PlanetScope and MODIS data

(1) PlanetScope. The orthorectified, near nadir view, level 3B surface reflectance product was accessed at https://www.planet.com/, including the quality control layer. We first generated a data quality mask based on the Unusable Data Mask (UDM) layer, following the instructions in Planet (2019). This default cloud masking, however, did not fully detect all cloud contamination. We therefore implemented a customized cloud/cloud-shadow removal algorithm that operated for each PlanetScope image, following Fraser et al. (2009) and Hillger and Clark (2002). This algorithm uses principal component analysis (PCA) (Chavez and Kwarteng, 1989) together with

Otsu thresholding (Otsu, 1979). After applying this additional clouds/cloud shadows quality control, we carefully checked and manually masked any remaining clouds and cloud shadows. This last step was labor intensive but developing a better automatic cloud/cloud-shadow removal algorithm is beyond the scope of this paper.

(2) MODIS. The MCD43A1 product was accessed at https://search.earthdata.nasa.gov/. This product provides the model parameters for removing the BRDF effect. We first adjusted the MCD43A1 reflectance to a nadir view, 0° relative azimuth angle and 45° solar zenith angle, following the technical guide at (https://www.umb.edu/spectralmass/terra_aqua_modis/v006/introduction). We then generated and applied the band-specific pixel QA layer that indicates high-quality band-specific BRDF inversion results (i.e. only using quality bit index = 0/1 for full/magnitude BRDF inversions) to retain as many good pixels (Schaaf et al., 2002, 2011). These procedures were applied to each pixel of daily MODIS data. Following Wu et al. (2018), we also applied the QA30 flag to further minimize cloud/aerosol impacts. This flag assumes that a pixel is most likely free from cloud/aerosol contamination when at least 30% of the pixels within a 5km×5km area centered on this pixel are also valid (i.e. passing through pixel QA control). Collectively, we applied QA30 when calculating the mean MODIS seasonality using all 20-year (2000-2019) data as well as calculating the seasonal trends for the MODIS data in 2018 and 2019 (to match with PlanetScope data for cross-calibration).

3.2 (Task 2): Cross-calibrating PlanetScope data using BRDF-adjusted MODIS

We divided this task into four sub-tasks described in sub-sections 3.2.1 through 3.2.4.

3.2.1 Retaining best quality MODIS data in 2018 and 2019

For this subtask, first, the band-specific quality control (including pixel QA and associated QA30 flag) was generated and applied to daily MODIS data in 2018 and 2019 to filter bad pixels with cloud/aerosol/cloud-shadow contaminations. Second, for each pixel of our study sites, we used all the MODIS data (2000-2019) to derive an annual cycle of band-specific means and their 95% confidence intervals at the daily timescale. This data had minimum cloud/aerosol contamination as it was sourced from a large selection of candidate pixels over time, and was then

used as an additional quality control to help filter any remaining bad pixels not previously removed in the MODIS 2018 and 2019 data.

3.2.2 Gap-filling MODIS time series in 2018 and 2019

High-quality paired satellite data of the same day were needed for cross-calibration but were not always available. To meet this need, we used the available best quality MODIS data for 2018 and 2019 (as described in Section 3.2.1 above), and developed a gap-filling method to gap fill those missing values in 2018 and 2019. MODIS gap-filling for these two years was performed on a daily, per band and per pixel level, following the three scenarios as follows:

i) if there were more than 200 valid daily measurements among a total of 365 measurements for a target MODIS pixel in 2018/2019, we then fitted a cubic spline curve to the data and used the daily fitted values for all days with missing values;

ii) if there were more than 50 but less than 200 valid daily measurements for a target MODIS pixel in 2018/2019, we turned to a reference (i.e. mean valid daily measurements from a neighboring 5km×5km area centered on the target pixel) to assist gap-filling, with two situations. If the current-year MODIS data (2018/2019) of the neighboring 5km×5km area had sufficient (≥200) mean valid daily measurements, the current-year data only was used to calculate the reference. Otherwise, all 20 years of data (2000-2009) were used to derive the reference. With the reference, we fitted its seasonal trend with a cubic spline curve to cover the full annual cycle. In order to preserve any real divergence between the target pixel and the average from its neighboring 5km×5km area, we then shifted the shape of the fitted reference curve up and down until it best matched with all the valid daily measurements of the target pixel in 2018/2019. We last interpolated those missing values of the target pixel based on the shifted curve.

iii) if there were less than 50 valid daily measurements for a target MODIS pixel in 2018/2019, we assumed each day's reflectance of the target pixel was the same as from 20-year daily mean of its neighboring 5km×5km area. We first fitted a cubic spline curve to the 20-year daily mean, and then used the daily fitted values to fill all missing values of the target pixel in 2018/2019.

Our Fig. S2 summarized the relative abundance of these three gap-filling scenarios. The first two gap-filling scenarios dominated (>99%) in our study.

Since a long-term (2000-2019) mean annual cycle was involved in our gap-filling procedures (i.e. scenarios ii and iii, above), in order to test whether it is fine to use this long-term mean annual cycle, we respectively examined the ecosystem-scale MODIS daily mean for 2018, 2019 and 2000-2019. As shown in Figs. 3 and S3, the curve of 2018/2019 and the curve of long-term mean are very similar, suggesting that the use of long-term mean annual cycle to aid our gap-filling processes is reasonable. Also in Figs. 3 and S3, the seasonal trend of gap-filled MODIS in 2018/2019 very well tracks that of original, non-gap-filled MODIS in 2018/2019, providing additional confidence on the reliability of our gap-filling method. Admittedly, there was an empirical choice of the thresholds (at 200 and 50 valid daily values per year) in determine gap-filling procedures. A further sensitivity test (Fig. S4), however, suggests that our gap-filling results are valid. For demonstration purpose, the original MODIS data with gaps and the corresponding gap-filled MODIS data are shown in the top and bottom panels of Fig. S5, respectively.

3.2.3 Cross-calibrating PlanetScope using band-specific histogram matching

PlanetScope was cross-calibrated to the (gap-filled) BRDF-adjusted MODIS of the same day using histogram matching—a commonly-used method for spectral cross-calibration of data acquired from different sensors (Chavez and Mackinnon, 1994; Yang and Lo, 2000). The cross-calibration was conducted for each band of each PlanetScope image. We first upscaled PlanetScope to the MODIS spatial resolution, and then calculated the pair of band-specific histograms respectively for MODIS and the upscaled PlanetScope. A Gaussian distribution was then applied to fit the histograms (Fig. 4). For each reflectance band, we adjusted the upscaled PlanetScope data to give the same mean and standard deviation as the corresponding band from BRDF-adjusted MODIS, using a linear transformation. We recorded the band-specific adjustment coefficients. We then applied these derived coefficients to the PlanetScope images at their original 3m resolution. Fig. S6 shows band-specific comparisons between PlanetScope data of pre and post cross-calibration. The calibrated PlanetScope data show less variability over the season compared to the original uncalibrated data.

3.2.4 Evaluating the robustness of the cross-calibration results

The robustness of our cross-calibration was evaluated by assessing the spectral consistency of permanent objects, i.e. the extracted building pixels at the Alter do Chão site that should have

stable reflectance spectra over a season after BRDF correction. Specifically, we manually identified about 180 building pixels in the PlanetScope images, and assessed the seasonal variability of their reflectance spectra prior and post cross-calibration.

3.3 (Task 3): Estimating NPV and GV fractions using linear spectral unmixing of calibrated PlanetScope

We hypothesized that there are three key elements within each forest canopy pixel (Fig. S1): NPV (bare illuminated branches), GV (illuminated green leaves) and shade (shadow caused by tall crowns and by deep narrow gaps). Our objective was to transform canopy reflectance of the four PlanetScope bands into variables with clear biophysical meaning. The variables of greatest interest were the NPV fraction and GV fraction. Details on the extraction of endmember-specific reflectance spectra and the linear spectral unmixing model follow.

(1) Extracting endmember-specific reflectance spectra. We followed an existing approach (Roberts et al., 1992) to extract endmember-specific reflectance spectra. It includes the following four steps. First, we applied a single principle component (PC) transformation to all calibrated PlanetScope data to summarize their 4-D band space in a 2-D scatter plot of PC1 and PC2, which resulted in a triangular point cloud (Fig. S7). Second, we performed careful visual assessments to manually identify pure pixels of each of the three endmembers, collecting at least 80 pixels per endmember from the calibrated PlanetScope images covering the full dry season. Third, we plotted and overlaid these manually identified pure endmembers on the scatter plot as in Fig. S7, to see if they coincided with the point cloud vertices, as required for unmixing. Also in Fig. S7, we then delimited the rectangle for each endmember based on the mean and two standard deviations of each PCA axis derived from those manually identified. Last, we calculated the average reflectance per band for all image pixels found within the three rectangles to derive reflectance spectra for the three endmembers. We compared these endmember-specific reflectance spectra to spectra derived from the smaller number of visually sampled pixels and the results were very comparable (Fig. S8).

(2) Estimating pixel-level NPV and GV fractions using a linear spectral unmixing model. With the derived endmember-specific reflectance spectra, we then applied a linear spectral unmixing model (Keshava and Mustard, 2002) to estimate the fractional cover of each endmember on a pixel-by-pixel basis for each PlanetScope image, assuming that the three endmembers

contribute to surface reflectance in a weight that is linearly proportional to their fractional cover within a pixel. The linear spectral unmixing model can be written as below:

$$x_i = \sum_{k=1}^{M} p_{ik} e_k + \epsilon_i \, , i = 1, \cdots, N \quad (1)$$

where p_{ik} is the fraction of endmember k in pixel i, e_k is the reflectance spectra of the kth endmember, M is the number of endmembers (M=3), ϵ_i is an error term, x_i is the reflectance spectra of pixel i, and N is the total number of pixels of a given PlanetScope image. The fractional values of this model satisfy the constraints

$$p_{ik} \geq 0 \; \forall k = 1, \cdots, M; \; \sum_{k=1}^{M} p_{ik} = 1. \quad (2)$$

After estimating endmember-specific fractions, including the fractional covers for k=1, 2, 3, respectively representing NPV, GV, and shade, we then re-assigned the shade fraction of each pixel to its NPV and GV components (see Eqns. 3 and 4), according to their initial, estimated fraction values in Eqn. 1. This is based on an assumption that shade effect happens equally to the NPV and GV elements.

$$p_{i1}' = p_{i1} + \frac{p_{i1}}{p_{i1}+p_{i2}} \times p_{i3} \quad (3)$$

$$p_{i2}' = p_{i2} + \frac{p_{i2}}{p_{i1}+p_{i2}} \times p_{i3} \quad (4)$$

where p_{i1}, p_{i2} and p_{i1}', p_{i2}' are the fractions of pure endmembers of NPV and GV in pixel i before and after reassignment of the shade fraction (p_{i3}). After this attribution of shade, we were left with two endmembers, NPV and GV, whose fractional contribution to each PlanetScope pixel sums to 1.0. We also applied the same linear spectral unmixing method, including endmember-specific reflectance spectra derived from calibrated PlanetScope, to the BRDF-adjusted MODIS data.

3.4 (Task 4): Evaluating the accuracy of PlanetScope-derived seasonal trends in NPV and GV fractions by comparing with field and phenocam measurements of leaf phenology

We evaluated linear regressions between ecosystem-scale PlanetScope-derived NPV and GV fractions over the six months (June to November) in 2018/2019 and three local phenology measurements, including: (i) field measurements of LAI, (ii) phenocam-based leafless tree-crown fraction, and (iii) phenocam-based leafy tree-crown fraction (=1-leafless tree crown fraction).

3.5 (Sensitivity analysis): Assessing the effects of non-matching time span or spatial coverage on the derived ecosystem-scale leaf phenology patterns

There are multiple datasets involved in this study. These vary in the year of measurement, the multi-year duration of measurement and the spatial extent. Therefore, it is important to assess whether such variations would impact the derived ecosystem-scale leaf phenology patterns. For this purpose, we assessed the effects of temporal duration/offset and of spatial extent, respectively, summarized as below:

(1) Evaluating the effect of temporal duration and temporal offset on the derived ecosystem-scale phenology. In this study, four datasets were used, including phenocam observations (daily in years 2010-2011), field LAI measurements (monthly in years 2000-2005), MODIS data (daily in years 2000-2019), and PlanetScope data (22 dates of measurements in 2018 and 16 dates in 2019). Based on these datasets, we first tested whether the measurements from different years and multi-year durations would affect ecosystem-scale phenology using daily raw, non-gap-filled MODIS. The sensitivity analysis shows that the (average) ecosystem-scale phenology trends in 2000-2005, 2010-2011, 2018 and 2019 are very similar, and are all close to the 20-year mean seasonality at our study site (Fig. S9a, b). The analysis thus suggests that our local observations, though collected in different time periods, are still very useful to help evaluate ecosystem-scale phenology in 2018 and 2019.

(2) Evaluating the effect of spatial extent on the derived ecosystem-scale phenology. Spatial extent also differs in our datasets, including phenocam (in an about 200m×300m area), field LAI measurements (in a 100m×100m area), MODIS (in a 10km×10km area) and PlanetScope (in a 10km×10km area). To test the effect of spatial extent, we used the calibrated PlanetScope data and respectively derived the ecosystem-scale average seasonal trend for windows of different sizes centered on the k67 eddy covariance tower: 100m×100m, 200m×300m, 500m×500m, 1km×1km, 3km×3km, 5km×5km, and 10km×10km. The sensitivity analysis shows that regardless of the spatial extent, the (average) ecosystem-scale seasonal trends are quite similar and comparable (Fig. S9c, d). This also suggests that local observations from phenocam and LAI have sufficient spatial coverage to represent ecosystem-scale phenology at k67.

4. Results

4.1 Cross-calibrating PlanetScope: robustness of the method and the seasonal trend

The robustness of our cross-calibration results was evaluated through the following three types of assessments: 1) at the forest ecosystem scale, the average seasonal variability of all bands

and of two vegetation indices (VIs), the normalized difference vegetation index (NDVI) and the enhanced vegetation index (EVI) (Figs. 5 and S10); 2) at the fine spatial scale, the seasonal trend in reflectance spectra of permanent objects (i.e. buildings) (Fig. 6); and 3) also at the fine scale, the spectral reflectance of three pure endmembers (NPV, GV, and shade) (Fig. 7).

In the first assessment, our results show that calibrated PlanetScope captures the same ecosystem-scale seasonal trends from June to November as BRDF-adjusted MODIS, a consistent pattern throughout all four spectral bands and both VIs (blue, green, red, NIR, NDVI, and EVI; Figs. 5 and S10). Uncalibrated PlanetScope also shows similar dry season increasing trends across four reflectance bands and two VIs, but is not in perfect agreement with that of MODIS, possibly due to a BRDF effect related to dry-season variation in solar elevation as well as the inconsistency in the DN scaling among different PlanetScope sensors. As a result, the uncalibrated PlanetScope reflectance values and their seasonal ranges are both higher than those of BRDF-adjusted MODIS (Figs. 5 and S10). For example, the dry season range of blue reflectance in BRDF-adjusted MODIS is only 0.003-0.035, but it is 0.014-0.098 for PlanetScope. Similarly, ranges of 0.017-0.06, 0.007-0.045, and 0.20-0.40 are found in BRDF-adjusted MODIS green, red and NIR reflectances respectively, while 0.020-0.110, 0.020-0.093, and 0.23-0.42 are found in the corresponding uncalibrated PlanetScope. The cross-calibration also reduces the PlanetScope fluctuation that departs from the overall uncalibrated seasonal trend. Such cross comparisons thus suggest that the PlanetScope surface reflectance data indeed requires cross-calibration, and the proposed method effectively cross-calibrates the PlanetScope data, resulting in the same seasonal trend as MODIS at the ecosystem scale.

In addition to the ecosystem-scale consistency, our two additional assessments also demonstrate that calibrated PlanetScope rigorously captures the seasonal trend in surface reflectance at the fine scale. The assessment from the permanent objects demonstrates that the cross-calibration stabilizes the reflectance spectra variability of the buildings at the fine scale. As shown in Fig. 6, after the cross-calibration, the buildings have nearly constant reflectance spectra across the full dry season from June to November. In contrast, prior to calibration, their reflectance spectra show large inter-month variability. Another assessment from endmember-specific reflectance spectra also suggests that the post-calibration reflectance spectra for each pure endmember (of 3m spatial scale of canopy surface) show small variation within each endmember,

while displaying large inter-endmember differences for all four reflectance bands (Fig. 7), providing further confidence on the robustness of our calibrated results at the fine scale.

Despite MODIS and calibrated PlanetScope having the same seasonal trend in ecosystem-scale reflectance as above, our results suggest that calibrated PlanetScope also provides rich and detailed phenological variations at the pixel level of 3m (Fig. 8). Particularly, PlanetScope captures large variability in reflectance dynamics at the fine scale across both space and time. Such observed high seasonal variability at the fine-scale might result from the fact that the tropical forest at k67 harbors high plant diversity, and tree individuals of different species or the same species but with different growth environments vary in their phenological events including both timing and magnitude.

4.2 Evaluating the seasonal trends in NPV and GV fractions derived from the calibrated PlanetScope data

We compared the PlanetScope-derived NPV fraction (and its complement, GV fraction) with phenocam and field LAI observations. Our results demonstrate that at the ecosystem-scale, the estimated seasonal trends in NPV fraction agree well with phenocam observations of leafless tree-crown fraction (R^2=0.82, p=0.014 for PlanetScope 2018 in Fig. 9a; R^2=0.73, p=0.030 for PlanetScope 2019 in Fig. S11a), all of which show a decreasing trend in NPV fraction throughout the full dry season. The absolute dry-season change in NPV fraction is also similar across all indicators from both phenocam and PlanetScope: about 10% decrease from June to November. Meanwhile, we also observed a modest absolute value difference between the two approaches, with the NPV fraction derived from PlanetScope consistently having ~5-10% higher fraction values than the phenocam observations. The alternative metric, GV fraction from calibrated PlanetScope, also shows the expected complimentary dry-season increasing trends with phenocam observations (R^2=0.82, p=0.014 for PlanetScope 2018 in Fig. 9b; R^2=0.73, p=0.030 for PlanetScope 2019 in Fig. S11b) and field LAI measurements (R^2=0.81, p=0.015 for PlanetScope 2018 in Fig. 9b; R^2=0.72, p=0.034 for PlanetScope 2019 in Fig. S11b). Additionally, the NPV fraction extracted from BRDF-adjusted MODIS using the same linear spectral unmixing model also shows the similar pattern as that from calibrated PlanetScope in 2018 (R^2=0.78, p=0.019; Fig. S12) but having closer relationships with phenocam observations of the same year in 2010-2011 (R^2=0.96, p=0.001; Fig. S12).

In addition, we assessed pixel-level (i.e. 3m resolution) seasonal variability in NPV fraction extracted from calibrated PlanetScope. Our results in Fig. 10 show that there are large seasonal variations in NPV fraction at the pixel level, with some pixels exhibiting a similar dry-season decreasing trend compared with the ecosystem-scale average pattern as shown in Fig. 9a but with large differences in change magnitude across pixels, while other pixels exhibit no trend or an increasing seasonal trend. Meanwhile, Fig. 11 provides the dry-season change rate in NPV fraction at the pixel level with a much greater decreasing trend than increasing trend in NPV fraction (84.6% vs. 15.4%) in the same area. Further, by assessing the seasonal changing trend across all the PlanetScope pixels at the k67 site, our results in Fig. S13 suggest that there are 71.2% (and 74.4%) of all pixels showing a dry-season decreasing trend in NPV fraction (i.e. a green-up) while 28.8% (and 25.6%) of all pixels showing a dry-season increasing trend (i.e. a brown-down) in 2018 (and 2019).

5. Discussion

Understanding patterns of plant phenology from individual tree-crowns up to ecosystems remains a critical challenge in plant ecology in general (Berra et al., 2019; Hufkens et al., 2012) and ecology of tropical evergreen forests in particular (Albert et al., 2018; Lopes et al., 2016; Park et al., 2019). In this study, we demonstrated that an integration of high-resolution PlanetScope with coarse-resolution MODIS improves characterization of dry-season phenostages and green-up of tropical evergreen forests across a wide range of spatial scales from a pixel of 3m (i.e. the scale of an individual tree-crown or below) up to ecosystems. Combined with a linear spectral unmixing model, such cross-satellite integration quantitatively differentiates GV from NPV, which is superior to conventional phenology monitoring using reflectance or a vegetation index because it has improved biophysical meaning. Our work thus represents a significant step forward in our ability to improve characterization of dry-season leaf phenology pattern in tropical evergreen forests, ranging from tree-crown scales to ecosystems and from conventional metrics of reflectance or vegetation index to GV and NPV fractions.

Our proposed PlanetScope-MODIS integration is similar in concept to previous cross-sensor fusion/calibration work, but with advances. As in prior fusion/calibration work (Gao et al., 2006; Houborg & McCabe, 2018a, 2018b), we used an orbital sensor of coarse spatial resolution that is frequent, accurate and corrected for BRDF effects as the benchmark to cross-calibrate a

552 high spatial resolution sensor with lower accuracy and uncorrected BRDF. We followed the
553 approach of Luo et al. (2018) to gap fill missing days for each pixel in the MODIS timeline
554 according to its own seasonal trend or the seasonal trends from adjacent pixels. Different from
555 previous fusion/calibration work, we did not gap fill the high spatial resolution sensor timeline,
556 because PlanetScope provides high frequency nadir-view coverage across the full dry season for
557 our site. Beyond these similarities and differences, our approach includes three major
558 advancements.

559 First, to our knowledge, it is the first study to integrate multiple sensors and orbital
560 platforms to improve fine-scale leaf phenology studies of tropical evergreen forest ecosystems.
561 Cross-scale multi-satellite integration has been challenging in tropical evergreen forests, due to the
562 frequent cloud cover over the annual cycle. Consequently, most satellite fusion/calibration
563 techniques have been developed and applied in other biomes (Liao et al., 2019; Semmens et al.,
564 2016; Walker et al., 2012; Yang et al., 2017) but has been less used in tropical biomes both in
565 techniques and mechanism for phenology monitoring (Viennois et al., 2013; Zeng et al., 2018).
566 Here we demonstrated the feasibility of integrating PlanetScope with MODIS for cross-scale
567 detection of tropical forest leaf phenology (Figs. 5 and 8). In contrast, the coarse-resolution
568 MODIS sensors alone can detect ecosystem-scale but not fine-scale leaf phenology dynamics.
569 Similarly, the use of the PlanetScope constellation alone is unsuccessful due to poor calibration
570 (Houborg & McCabe, 2018a, 2018b) and seasonally varying solar elevation, leading to noisy and
571 biased reflectance values over the season, impeding leaf phenology monitoring at both ecosystem
572 and tree-crown scales (Figs. 5 and 6). Only with the PlanetScope-MODIS integration, we detected
573 the dry season leaf phenology dynamics at both ecosystem (i.e. an overall dry-season green-up
574 pattern) and individual tree-crown (i.e. pronounced phenological diversity among individuals)
575 scales. These remotely detected phenology patterns agree with many previous findings from field
576 (e.g. Brando et al., 2010), tower-phenocam (e.g. Wu et al., 2016), and satellite (e.g. Huete et al.,
577 2006; Saleska et al., 2016) observations. For example, we confirm that Central Amazon evergreen
578 forests undergo leaf turnover (as indicated by many pre-flush leafless phenostage crowns)
579 followed by ecosystem-scale green-up (due to post-flush leaf maturation) in the dry season period
580 of high sunlight and reduced rainfall (Wu et al., 2018). This suggests that these forests are not
581 water limited and are more likely light limited (Guan et al., 2015; Huete et al., 2006). However, it
582 remains mechanistically unclear and awaits more in-depth future exploration regarding why there

583 is such high inter-crown phenological diversity during the long dry-season (Figs. 10-11), despite
584 an overall ecosystem-scale green-up pattern (Fig. 9).

585 The success of our multi-sensor integration relies, first of all, on several conditions: i)
586 MODIS has long-term frequent measurements, which provides sufficient observations to obtain
587 cloud-free samples over annual cycles. Thus it is feasible to use the mean seasonal trend to help
588 interpolate missing daily values due to cloud/aerosol/cloud shading contamination; ii) MODIS
589 BRDF-adjusted products have been rigorously validated previously (Maeda et al., 2016; Wagner
590 et al., 2016; Wu et al., 2018), and thus can serve as a good reference for benchmarking other
591 satellites, such as PlanetScope shown in this study (Fig. 6); and iii) PlanetScope has frequent
592 measurements over the annual cycles, e.g. nearly daily revisit cycle, which also makes it feasible
593 to obtain frequent cloud-free data, especially during the less cloudy dry season (Fig. 5). The
594 success of our integration also suggests that the same approach might be extendable to Sentinel-2
595 (with 5day interval, 10m resolution) (Drusch et al., 2012) and other satellites with both frequent
596 revisit and high spatial resolution (e.g. GeoEye-1, GaoFen-2, VENuS and Pleiades) (Dedieu et al,
597 2006; Dribault et al., 2012; Gu and Tong, 2015; Pu et al., 2018). We recommend BRDF-adjusted
598 MODIS be used as a calibration reference for such multi-sensor integration.

599 Second, we applied rigorous assessments to ensure such PlanetScope-MODIS integration
600 worked consistently well across all scales. The calibrated PlanetScope data exhibited the same
601 seasonal pattern as MODIS at the ecosystem scale (e.g. green lines in Fig. 5). However, this alone
602 does not prove the cross-calibration also works at the fine spatial scale. For validation of fine-scale
603 we performed one additional assessment which is the post-calibration spectral stability over the
604 entire dry season for permanent objects (i.e. buildings) (Fig. 6b). The other is the assessment of
605 endmember-specific reflectance spectra (NPV, GV, and shade) extracted from the calibrated
606 PlanetScope data (Fig. 7). These endmember-specific reflectance spectra agree well with previous
607 findings based on field measurements of reflectance spectra of the three canopy materials (Asner,
608 1998; Clark and Roberts, 2012), with other high-resolution satellite data (Feret et al., 2015), and
609 with process-based model simulations (Wu et al., 2018). In summary, a multitude of validation
610 assessments suggest the proposed PlanetScope-MODIS integration works consistently well at both
611 fine and ecosystem scales. Additionally, because stable building reflectance spectra and NPV and
612 GV fractions were extracted on the PlanetScope pixel level of 3m, we conclude the cross-
613 calibration allows detection of tree-crown scale phenostages.

Third, our approach provides a metric with clear biophysical meaning, the NPV fraction or its complement, the GV fraction, to aid quantitative measurements of tropical leaf phenology. Satellite remote sensing has been powerful to monitor land surface phenology over large areas (Moulin et al., 1997; White et al., 2009), but lacks clear biophysical meaning if expressed as canopy reflectance, or even as a vegetation index (Samanta et al., 2012; Wu et al., 2018). The timing of massive leaf flush and of complete or partial loss are important phenostages at the tree-crown scale and are detectable using canopy leaf fractional cover (Lopes et al., 2016; Richardson et al., 2018). Based on this idea, we derived the NPV fraction to represent fractional cover of non-photosynthetic vegetation within a PlanetScope pixel using linear spectral unmixing. Our derived dry-season NPV trends demonstrate strong ecosystem-scale agreement with phenocam observations (Fig. 9) while also characterize large inter-crown variance at the fine-scale (Figs. 10-11), highlighting the effectiveness of our approach.

It is also worthy to note that there is some consistent seasonal mismatch in the absolute value of NPV fraction between phenocam and PlanetScope (Fig. 9). We hypothesize two main reasons for this mismatch. First, the NPV endmember spectra derived from 3-m PlanetScope data might differ from laboratory spectra of pure bare branch material. As a result, green leaves of shorter crowns (i.e. understory) are in the background of a single bare crown and the leaves of surrounding green crowns strongly transmit and reflect NIR preferentially onto an isolated bare crown, raising apparent NIR reflectance in the PlanetScope-derived NPV endmember (Eriksson et al., 2006). This leads to an overestimate of NPV fraction as part of green leaf information is assigned to the NPV category in a linear spectral unmixing. Second, though the seasonal trend in bare crown exposure was well correlated between the phenocam years of 2010-2011 and the PlanetScope year of 2018/2019, there could be a difference in magnitude between these two time periods (e.g. Fig. S12). Therefore, a further detailed monitoring and validation of tree-crown scale leaf phenology (e.g. using drones; Park et al., 2019) is still needed, but beyond the scope of this paper. Dry-season flowering in tropical trees (e.g. Borchert et al., 2005; Carvalho et al., 2013) might also affect the estimation of NPV fraction. Whether the flowering would lead to an overestimate of NPV fraction remains unknown, so more in-situ measurements of both flower phenology and canopy reflectance of flowering canopies are still needed to help quantify the flowering impacts. Nonetheless, flowers in the crowns of most Central Amazon trees occupy a small fraction of crown area, and a recent study (Lopes et al., 2016) using a tower-mounted

phenocam in a Central Amazon forest near Manaus, Brazil found that flowers have little effect on the seasonal change in ecosystem-scale "greenness".

The proposed PlanetScope-MODIS integration for assessments of seasonal and spatial dynamics in NPV fraction at the tree-crown scale also brings new opportunities to advance plant ecology studies. First, it can improve our understanding of phenological scaling from individuals to ecosystems (Nijland et al., 2016; Vrieling et al., 2017). Since ecosystem-scale phenology emerges from the phenology of a community of tree species and individuals, several recent studies have shown that the diversity in plant phenology at the fine scale can significantly affect the ecosystem-scale phenology extracted, including the timing of key phenological events (e.g. leaf on and off) (Chen et al., 2018) and the magnitude of seasonal fluctuations (e.g. Lopes et al., 2016; Saleska et al., 2016). This not only applies to the temperate biomes, where ecosystem-scale phenology shows large sensitivity to global climate change (Jeong et al., 2011; Körner and Basler, 2010; Thackeray et al., 2016), but is also important for the tropical biomes, where phenological dynamics at the tree-crown level dominantly determine tropical forests' ability to interact with the climate system (e.g. Albert et al., 2018; Wright et al., 2017; Wu et al., 2016). The improved fine-scale phenology monitoring as shown here thus offers a great opportunity to revisit these scaling issues. Second, fine-scale NPV assessments also provide an important dataset to help parameterize, constrain, and evaluate process-based models. Leaf phenology has been an important component for process-based models to simulate large-scale climate-vegetation interactions (Fisher et al., 2015; Restrepo-Coupe et al., 2017; Richardson et al., 2012). Yet the patterns and mechanisms of leaf phenology over large scales remain poorly understood (Richardson et al., 2010; Xu et al., 2016, 2017). Once leaf phenology patterns have been derived at both fine and ecosystem scales, it becomes possible to evaluate the competing mechanisms underlying current phenology models and to parameterize process-based models for cross-scale simulations of carbon and water fluxes.

Despite these promising implications, our study also identifies four important next steps that need to be considered for future advances. First, the robustness of this method in the wet season is not yet assessed due to the frequent cloud covers in the high rainfall wet season of our study site. There might be even fewer or no valid pixels for both MODIS and PlanetScope measurements, resulting in higher uncertainty for MODIS gap-filling results in the wet season and insufficient PlanetScope pixels for spectral cross-calibration using the histogram matching approach (Fig.3). To (partly) resolve this issue, we recommend a stricter quality control for

MODIS and an improved cloud removal algorithm for PlanetScope (e.g. Planet's UDM2 classification approach; Shendryk et al., 2019) to retain as many valid pixels and/or PlanetScope in a monthly composite (assuming unchanged leaf phenology within a month) be needed to ensure sufficient valid pixels for spectral cross-calibration. Second, the topography effects are not yet considered in this study. Across large tropical areas, there are large variations in topography (Jucker et al., 2018; Schwartz et al., 2019). Slope and aspect of the land relative to view and illumination angles exert large effects on apparent land surface reflectance (Matsushita et al., 2007; Wu et al., 2019a, 2019b). To avoid these complications, we focused on a large flat plateau site in the current study. But it is thus important to explore whether the same method can be extended to other regions with more accentuated topographic variation. Third, we used a fixed PlanetScope-derived, endmember-specific reflectance spectra in linear spectral unmixing. Other unmixing models (Asner et al., 2009; Roberts et al., 1998) accommodate variation in the reflectance spectra of each endmember. Allowing for such variation is important for deriving a more broadly applicable approach across large tropical areas. Fourth, our multi-sensor integration can enable high-resolution monitoring of dry season dynamics in canopy-surface NPV and GV fractions. However, it remains difficult to separate each individual tree crowns. Therefore, any approach to enable tree-crown segregation or to combine other high-resolution orthorectified images (e.g. drone or aerial photos) for tree-crown segregation (Klosterman et al., 2018; Park et al., 2019) will make the derived fine-scale phenology metrics more useful.

6. Conclusions

This study develops a method to integrate PlanetScope with BRDF-adjusted MODIS to enable cross-scale phenology monitoring in a Central Amazon tropical evergreen forest. The method shares a similar concept as previous satellite image cross-sensor fusion/calibration work, but also has three major advancements. First, it represents the first study in tropical evergreen forests to integrate multi-satellites to enable fine-scale phenology monitoring. Second, we adopted rigorous validation assessments to ensure that PlanetScope-MODIS integration worked consistently well across all spatial scales. Third, the method also offers a metric with clear biophysical meaning, i.e. the NPV fraction, to aid quantification of tropical leaf phenology. Compared with other phenology monitoring methods, such as tower-mounted phenocams and frequent drone flights, our integration not only aids detection of tree-crown scale leaf phenology

with high accuracy (R^2=0.82; Fig. 9), but also allows for leaf phenology monitoring to much larger areas. These advantages make our method can be extended to other high resolution satellites and/or other regions, advancing our ability to monitor land plant phenology and associated vegetation dynamics in the context of global change.

Acknowledgements: J. Wang, S. W., Z. Y. and J. Wu were supported by HKU research startup fund awarded to J. Wu. D. Y. was supported by the Next-Generation Ecosystem Experiments (NGEE-Tropics) project that is supported by the Office of Biological and Environmental Research in the Department of Energy, Office of Science, and through the United States Department of Energy contract No. DE-SC001704 to Brookhaven National Laboratory. M.C. is supported by a Laboratory Directed Research & Development program of Pacific Northwest National Laboratory, US Department of Energy. The PlanetScope data were accessed through the Education and Research Program, contracted between Planet Labs Inc. and HKU.

References:

Albert, L.P., Restrepo-Coupe, N., Smith, M.N., Wu, J., Chavana-Bryant, C., Prohaska, N., Taylor, T.C., Martins, G.A., Ciais, P., Mao, J.F., Arain, M.A., Li, W., Shi, X.Y., Ricciuto, D.M., Huxman, T.E., McMahon, S.M., Saleska, S.R., 2019. Cryptic phenology in plants: Case studies, implications, and recommendations. Global change biology, 25, 3591-3608.

Albert, L.P., Wu, J., Prohaska, N., de Camargo, P.B., Huxman, T.E., Tribuzy, E.S., Ivanov, V.Y., Oliveira, R.S., Garcia, S., Smith, M.N., Oliveira, R.C., Restrepo-Coupe, N., da Silva, R., Stark, S.C., Martins, G.A., Penha, D.V., Saleska, S.R., 2018. Age-dependent leaf physiology and consequences for crown-scale carbon uptake during the dry season in an Amazon evergreen forest. New Phytologist, 219, 870-884.

Alberton, B., Torres, R.D., Cancian, L.F., Borges, B.D., Almeida, J., Mariano, G.C., dos Santos, J., Morellatoa, L.P.C., 2017. Introducing digital cameras to monitor plant phenology in the tropics: Applications for conservation. Perspectives in Ecology and Conservation, 15, 82-90.

Asner, G.P., 1998. Biophysical and biochemical sources of variability in canopy reflectance. Remote Sensing of Environment, 64, 234-253.

Asner, G. P., Knapp, D. E., Balaji, A., Páez-Acosta, G., 2009. Automated mapping of tropical deforestation and forest degradation: CLASlite. Journal of Applied Remote Sensing, 3, 033543. http://doi.org/10.1117/1.3223675.

Berra, E.F., Gaulton, R., Barr, S., 2019. Assessing spring phenology of a temperate woodland: A multiscale comparison of ground, unmanned aerial vehicle and Landsat satellite observations. Remote Sensing of Environment, 223, 229-242.

Blanchard, E., Birnbaum, P., Ibanez, T., Boutreux, T., Antin, C., Ploton, P., Vincent, G., Pouteau, R., Vandrot, H., Hequet, V., Barbier, N., Droissart, V., Sonke, B., Texier, N., Kamdem, N.G., Zebaze, D., Libalah, M., Couteron, P., 2016. Contrasted allometries between stem diameter, crown area, and tree height in five tropical biogeographic areas. Trees-Structure and Function, 30, 1953-1968.

747 Bonan, G. B., 2008. Forests and climate change: forcings, feedbacks, and the climate benefits of forests.
748 science, 320, 1444-1449.
749 Borchert, R., Renner, S.S., Calle, Z., Navarrete, D., Tye, A., Gautier, L., Spichiger, R., von Hildebrand, P.,
750 2005. Photoperiodic induction of synchronous flowering near the Equator. Nature, 433, 627–629.
751 Brando, P.M., Goetz, S.J., Baccini, A., Nepstad, D.C., Beck, P.S.A., Christman, M.C., 2010. Seasonal and
752 interannual variability of climate and vegetation indices across the Amazon. Proceedings of the
753 National Academy of Sciences of the United States of America, 107, 14685-14690.
754 Carvalho, S., Schlerf, M., van Der Putten, W. H., and Skidmore, A. K., 2013. Hyperspectral reflectance of
755 leaves and flowers of an outbreak species discriminates season and successional stage of
756 vegetation. International journal of applied earth observation and geoinformation, 24, 32-41.
757 Chavez, P.S., Kwarteng, A.Y., 1989. Extracting spectral contrast in Landsat Thematic Mapper image data
758 using selective principal component analysis. Photogrammetric Engineering and Remote Sensing, 55,
759 339-348.
760 Chavez, P.S., Mackinnon, D.J., 1994. Automatic detection of vegetation changes in the southwestern
761 United States using remotely sensed images. Photogrammetric Engineering and Remote Sensing, 60,
762 571-583.
763 Chen, X., Wang, D.W., Chen, J., Wang, C., Shen, M.G., 2018. The mixed pixel effect in land surface
764 phenology: A simulation study. Remote Sensing of Environment, 211, 338-344.
765 Clark, M.L., Roberts, D.A., 2012. Species-level differences in hyperspectral metrics among tropical
766 rainforest trees as determined by a tree-based classifier. Remote Sensing, 4, 1820-1855.
767 de Moura, Y.M., Galvao, L.S., Hilker, T., Wu, J., Saleska, S., do Amaral, C.H., Nelson, B.W., Lopes, A.P.,
768 Wiedeman, K.K., Prohaska, N., de Oliveira, R.C., Machado, C.B., Aragao, L.E.O.C., 2017. Spectral
769 analysis of amazon canopy phenology during the dry season using a tower hyperspectral camera and
770 modis observations. ISPRS Journal of Photogrammetry and Remote Sensing, 131, 52-64.
771 Dedieu G., Karnieli A., Hagolle O., Jeanjean H., Cabot F., Ferrier P., Yaniv Y., 2006. Venμs : A joint
772 Israel-French Earth Observation scientific mission with high spatial and temporal resolution
773 capabilities. In: The 2nd International Symposium on Recent Advances in Qualitative Remote Sensing,
774 pp. 517-521.
775 Detto, M., Wright, S.J., Calderon, O., Muller-Landau, H.C., 2018. Resource acquisition and reproductive
776 strategies of tropical forest in response to the El Niño-Southern Oscillation. Nature Communications,
777 9, 913. http://doi.org/10.1038/s41467-018-03306-9.
778 Dribault, Y., Chokmani, K., Bernier, M., 2012. Monitoring seasonal hydrological dynamics of
779 minerotrophic peatlands using multi-date GeoEye-1 very high resolution imagery and object-based
780 classification. Remote Sensing, 4, 1887-1912.
781 Drusch, M., Del Bello, U., Carlier, S., Colin, O., Fernandez, V., Gascon, F., Hoersch, B., Isola, C., Laberinti,
782 P., Martimort, P., Meygret, A., Spoto, F., Sy, O., Marchese, F., Bargellini, P., 2012. Sentinel-2: ESA's
783 Optical High-Resolution Mission for GMES Operational Services. Remote Sensing of Environment,
784 120, 25-36.
785 Eamus, D., 1999. Ecophysiological traits of deciduous and evergreen woody species in the seasonally dry
786 tropics. Trends in Ecology & Evolution, 14, 11-16.
787 Eriksson, H.M., Eklundh, L., Kuusk, A., Nilson, T., 2006. Impact of understory vegetation on forest canopy
788 reflectance and remotely sensed LAI estimates. Remote Sensing of Environment. 103. 408-418.
789 http://doi.org/10.1016/j.rse.2006.04.005.
790 Feret, J.B., Corbane, C., Alleaume, S., 2015. Detecting the phenology and discriminating Mediterranean
791 natural habitats with multispectral sensors-An analysis based on multiseasonal field spectra. IEEE
792 Journal of Selected Topics in Applied Earth Observations and Remote Sensing, 8, 2294-2305.
793 Fisher, R.A., Muszala, S., Verteinstein, M., Lawrence, P., Xu, C., McDowell, N.G., Knox, R.G., Koven,
794 C., Holm, J., Rogers, B.M., Spessa, A., Lawrence, D., Bonan, G., 2015. Taking off the training wheels:
795 The properties of a dynamic vegetation model without climate envelopes, CLM4.5(ED). Geoscientific
796 Model Development, 8, 3593-3619.

797 Fraser, A. D., Massom, R. A., Michael, K. J., 2009. A method for compositing polar MODIS satellite
798 images to remove cloud cover for landfast sea-ice detection. IEEE transactions on geoscience and
799 remote sensing, 47, 3272-3282.
800 Galvao, L.S., dos Santos, J.R., Roberts, D.A., Breunig, F.M., Toomey, M., de Moura, Y.M., 2011. On intra-
801 annual EVI variability in the dry season of tropical forest: A case study with MODIS and hyperspectral
802 data. Remote Sensing of Environment, 115, 2350-2359.
803 Gao, F., Masek, J., Schwaller, M., Hall, F., 2006. On the blending of the Landsat and MODIS surface
804 reflectance: Predicting daily Landsat surface reflectance. IEEE Transactions on Geoscience and
805 Remote Sensing, 44, 2207-2218.
806 Gonçalves, N. B., Lopes, A. P., Dalagnol, R., Wu, J., Pinho, D. M., Nelson, B. W., 2020. Both near-surface
807 and satellite remote sensing confirm drought legacy effect on tropical forest leaf phenology after
808 2015/2016 ENSO drought. Remote Sensing of Environment, 237, 111489.
809 http://doi.org/10.1016/j.rse.2019.111489.
810 Gu, X.F., Tong, X.D., 2015. Overview of China Earth Observation Satellite Programs. IEEE Geoscience
811 and Remote Sensing Magazine, 3, 113-129.
812 Guan, K.Y., Pan, M., Li, H.B., Wolf, A., Wu, J., Medvigy, D., Caylor, K.K., Sheffield, J., Wood, E.F.,
813 Malhi, Y., Liang, M.L., Kimball, J.S., Saleska, S.R., Berry, J., Joiner, J., Lyapustin, A.I., 2015.
814 Photosynthetic seasonality of global tropical forests constrained by hydroclimate. Nature Geoscience,
815 8, 284-289.
816 Hillger, D. W., Clark, J. D., 2002. Principal component image analysis of MODIS for volcanic ash. Part I:
817 Most important bands and implications for future GOES imagers. Journal of Applied Meteorology, 41,
818 985-1001.
819 Houborg, R., McCabe, M. F., 2018a. A cubesat enabled spatio-temporal enhancement method (cestem)
820 utilizing planet, landsat and modis data. Remote Sensing of Environment, 209, 211-226.
821 Houborg, R., McCabe, M. F., 2018b. Daily Retrieval of NDVI and LAI at 3 m Resolution via the Fusion
822 of CubeSat, Landsat, and MODIS Data. Remote Sensing, 10, 890. https://doi.org/10.3390/rs10060890.
823 Huete, A.R., Didan, K., Miura, T., Rodriguez, E.P., Gao, X., Ferreira, L.G., 2002. Overview of the
824 radiometric and biophysical performance of the MODIS vegetation indices. Remote Sensing of
825 Environment, 83, 195-213.
826 Huete, A.R., Didan, K., Shimabukuro, Y.E., Ratana, P., Saleska, S.R., Hutyra, L.R., Yang, W.Z., Nemani,
827 R.R., Myneni, R., 2006. Amazon rainforests green-up with sunlight in dry season. Geophysical
828 Research Letters, 33, L06405. https://doi.org/10.1029/2005GL025583.
829 Hufkens, K., Friedl, M., Sonnentag, O., Braswell, B.H., Milliman, T., Richardson, A.D., 2012. Linking
830 near-surface and satellite remote sensing measurements of deciduous broadleaf forest phenology.
831 Remote Sensing of Environment, 117, 307-321.
832 Hutyra, L.R., Munger, J.W., Saleska, S.R., Gottlieb, E., Daube, B.C., Dunn, A.L., Amaral, D.F., de
833 Camargo, P.B., Wofsy, S.C., 2007. Seasonal controls on the exchange of carbon and water in an
834 Amazonian rain forest. Journal of Geophysical Research, 112,
835 G03008. https://doi.org/10.1029/2006JG000365.
836 Jeong, S.J., Ho, C.H., Gim, H.J., Brown, M.E., 2011. Phenology shifts at start vs. end of growing season in
837 temperate vegetation over the Northern Hemisphere for the period 1982-2008. Global Change Biology,
838 17, 2385-2399.
839 Jucker, T., Bongalov, B., Burslem, D.F.R.P., Nilus, R., Dalponte, M., Lewis, S.L., Phillips, O.L., Qie, L.,
840 Coomes, D.A., 2018. Topography shapes the structure, composition and function of tropical forest
841 landscapes. Ecology Letters, 21, 989-1000.
842 Jung, M., Schwalm, C., Migliavacca, M., Walther, S., Camps-Valls, G., Koirala, S., Anthoni, P., Besnard,
843 S., Bodesheim, P., Carvalhais, N., Chevallier, F., Gans, F., Groll, D. S., Haverd, V., Ichii, K., Jain, A.
844 K., Liu, J., Lombardozzi, D., Nabel, J. E. M. S., Nelson, J. A., Pallandt, M., Papale, D., Peters, W.,
845 Pongratz, J., Rödenbeck, C., Sitch, S., Tramontana, G., Weber, U., Reichstein, M., Koehler, P.,
846 O'Sullivan, M., and Walker, A., 2019. Scaling carbon fluxes from eddy covariance sites to globe:

Synthesis and evaluation of the FLUXCOM approach, Biogeosciences Discuss. https://doi.org/10.5194/bg-2019-368.
Keshava, N., Mustard, J.F., 2002. Spectral unmixing. IEEE Signal Processing Magazine, 19, 44-57.
Klosterman, S., Melaas, E., Wang, J.A., Martinez, A., Frederick, S., O'Keefe, J., Orwig, D.A., Wang, Z.S., Sun, Q.S., Schaaf, C., Friedl, M., Richardson, A.D., 2018. Fine-scale perspectives on landscape phenology from unmanned aerial vehicle (UAV) photography. Agricultural and Forest Meteorology, 248, 397-407.
Körner, C., Basler, D., 2010. Phenology Under Global Warming. Science, 327, 1461-1462.
Liao, C., Wang, J., Dong, T., Shang, J., Liu, J., Song, Y., 2019. Using spatio-temporal fusion of Landsat-8 and MODIS data to derive phenology, biomass and yield estimates for corn and soybean. Science of The Total Environment, 650, 1707-1721.
Lopes, A.P., Nelson, B.W., Wu, J., Graca, P.M.L.D., Tavares, J.V., Prohaska, N., Martins, G.A., Saleska, S.R., 2016. Leaf flush drives dry season green-up of the Central Amazon. Remote Sensing of Environment, 182, 90-98.
Luo, Y.N., Guanb, K.Y., Pen, J., 2018. STAIR: A generic and fully-automated method to fuse multiple sources of optical satellite data to generate a high-resolution, daily and cloud-/gap-free surface reflectance product. Remote Sensing of Environment, 214, 87-99.
Maeda, E.E., Moura, Y.M., Wagner, F., Hilker, T., Lyapustin, A.I., Wang, Y.J., Chave, J., Mottus, M., Aragao, L.E.O.C., Shimabukuro, Y., 2016. Consistency of vegetation index seasonality across the Amazon rainforest. International Journal of Applied Earth Observation and Geoinformation, 52, 42-53.
Matsushita, B., Yang, W., Chen, J., Onda, Y., Qiu, G.Y., 2007. Sensitivity of the Enhanced Vegetation Index (EVI) and Normalized Difference Vegetation Index (NDVI) to topographic effects: A case study in high-density cypress forest. Sensors, 7, 2636-2651.
Moore, C.E., Brown, T., Keenan, T.F., Duursma, R.A., van Dijk, A.I.J.M., Beringer, J., Culvenor, D., Evans, B., Huete, A., Hutley, L.B., Maier, S., Restrepo-Coupe, N., Sonnentag, O., Specht, A., Taylor, J.R., van Gorsel, E., Liddell, M.J., 2016. Reviews and syntheses: Australian vegetation phenology: New insights from satellite remote sensing and digital repeat photography. Biogeosciences, 13, 5085-5102.
Morton, D.C., Nagol, J., Carabajal, C.C., Rosette, J., Palace, M., Cook, B.D., Vermote, E.F., Harding, D.J., North, P.R.J., 2014. Amazon forests maintain consistent canopy structure and greenness during the dry season. Nature, 506, 221-224.
Moulin, S., Kergoat, L., Viovy, N., Dedieu, G., 1997. Global-scale assessment of vegetation phenology using NOAA/AVHRR satellite measurements. Journal of Climate, 10, 1154-1170.
Nijland, W., Bolton, D.K., Coops, N.C., & Stenhouse, G., 2016. Imaging phenology; scaling from camera plots to landscapes. Remote Sensing of Environment, 177, 13-20.
Otsu, N., 1979. Threshold selection method from gray-level histograms. IEEE Transactions on Systems Man and Cybernetics, 9, 62-66.
Park, J.Y., Muller-Landau, H.C., Lichstein, J.W., Rifai, S.W., Dandois, J.P., Bohlman, S.A., 2019. Quantifying leaf phenology of individual trees and species in a tropical forest using unmanned aerial vehicle (UAV) Images. Remote Sensing, 11, 1534. https://doi.org/10.3390/rs11131534.
Planet, 2019. Planet Imagery Product Specification [WWW Document]. https://assets.planet.com/docs/combined-imagery-product-spec-april-2019.pdf (accessed 03 March 2020).
Planet Team, 2018. Planet Application Program Interface: In Space for Life on Earth. In. San Francisco, CA. https://api.planet.com (accessed 02 March 2020).
Pu, R.L., Landry, S., Yu, Q.Y., 2018. Assessing the potential of multi-seasonal high resolution Pleiades satellite imagery for mapping urban tree species. International Journal of Applied Earth Observation and Geoinformation, 71, 144-158.
Reich, P. B., 1995. Phenology of tropical forests: patterns, causes, and consequences. Canadian Journal of Botany, 73, 164–174. https://doi.org/10.1139/b95-020.

Restrepo-Coupe, N., da Rocha, H.R., Hutyra, L.R., da Araujo, A.C., Borma, L.S., Christoffersen, B., Cabral, O.M.R., de Camargo, P.B., Cardoso, F.L., da Costa, A.C.L., Fitzjarrald, D.R., Goulden, M.L., Kruijt, B., Maia, J.M.F., Malhi, Y.S., Manzi, A.O., Miller, S.D., Nobre, A.D., von Randow, C., Sa, L.D.A., Sakai, R.K., Tota, J., Wofsy, S.C., Zanchi, F.B., Saleska, S.R., 2013. What drives the seasonality of photosynthesis across the Amazon basin? A cross-site analysis of eddy flux tower measurements from the Brasil flux network. Agricultural and Forest Meteorology, 182, 128-144.

Restrepo-Coupe, N., Levine, N.M., Christoffersen, B.O., Albert, L.P., Wu, J., Costa, M.H., Galbraith, D., Imbuzeiro, H., Martins, G., da Araujo, A.C., Malhi, Y.S., Zeng, X.B., Moorcroft, P., Saleska, S.R., 2017. Do dynamic global vegetation models capture the seasonality of carbon fluxes in the Amazon basin? A data-model intercomparison. Global Change Biology, 23, 191-208.

Rice, A.H., Pyle, E.H., Saleska, S.R., Hutyra, L., Palace, M., Keller, M., de Camargo, P.B., Portilho, K., Marques, D.F., Wofsy, S.C., 2004. Carbon balance and vegetation dynamics in an old-growth Amazonian forest. Ecological Applications, 14, 55-71.

Richardson, A.D., Anderson, R.S., Arain, M.A., Barr, A.G., Bohrer, G., Chen, G.S., Chen, J.M., Ciais, P., Davis, K.J., Desai, A.R., Dietze, M.C., Dragoni, D., Garrity, S.R., Gough, C.M., Grant, R., Hollinger, D.Y., Margolis, H.A., McCaughey, H., Migliavacca, M., Monson, R.K., Munger, J.W., Poulter, B., Raczka, B.M., Ricciuto, D.M., Sahoo, A.K., Schaefer, K., Tian, H.Q., Vargas, R., Verbeeck, H., Xiao, J.F., Xue, Y.K., 2012. Terrestrial biosphere models need better representation of vegetation phenology: Results from the North American Carbon Program Site Synthesis. Global Change Biology, 18, 566-584.

Richardson, A.D., Black, T.A., Ciais, P., Delbart, N., Friedl, M.A., Gobron, N., Hollinger, D.Y., Kutsch, W.L., Longdoz, B., Luyssaert, S., Migliavacca, M., Montagnani, L., Munger, J.W., Moors, E., Piao, S.L., Rebmann, C., Reichstein, M., Saigusa, N., Tomelleri, E., Vargas, R., Varlagin, A., 2010. Influence of spring and autumn phenological transitions on forest ecosystem productivity. Philosophical Transactions of the Royal Society B, 365, 3227-3246.

Richardson, A.D., Hufkens, K., Milliman, T., Aubrecht, D.M., Chen, M., Gray, J.M., Johnston, M.R., Keenan, T.F., Klosterman, S.T., Kosmala, M., Melaas, E.K., Friedl, M.A., Frolking, S., 2018. Tracking vegetation phenology across diverse North American biomes using PhenoCam imagery. Scientific Data, 5, 180028. https://doi.org/10.1038/sdata.2018.28.

Roberts, D. A., Gardner, M., Church, R., Ustin, S., Scheer, G., Green, R. O., 1998. Mapping chaparral in the Santa Monica Mountains using Multiple Endmember Spectral Mixture models. Remote Sensing of Environment, 65, 267–279.

Roberts, D. A., Smith, M. O., Sabol, D. E., Adams, J. B., and Ustin, S. L., 1992. Mapping the spectral variability in photosynthetic and non-photosynthetic vegetation, soils, and shade using AVIRIS. In: Summaries 3rd Annual JPL Airborne Geoscience Workshop, pp 38–40.

Saleska, S.R., Wu, J., Guan, K.Y., Araujo, A.C., Huete, A., Nobre, A.D., Restrepo-Coupe, N., 2016. Dry-season greening of Amazon forests. Nature, 531, E4-E5. https://doi.org/10.1038/nature16457.

Samanta, A., Ganguly, S., Hashimoto, H., Devadiga, S., Vermote, E., Knyazikhin, Y., Nemani, R.R., Myneni, R.B., 2010. Amazon forests did not green-up during the 2005 drought. Geophysical Research Letters, 37. http:// doi.org/10.1029/2009GL042154.

Samanta, A., Ganguly, S., Vermote, E., Nemani, R.R., Myneni, R.B., 2012. Interpretation of variations in MODIS-measured greenness levels of Amazon forests during 2000 to 2009. Environmental Research Letters, 7, 024018. https://doi.org/10.1088/1748-9326/7/2/024018.

Schaaf, C.B., Gao, F., Strahler, A.H., Lucht, W., Li, X.W., Tsang, T., Strugnell, N.C., Zhang, X.Y., Jin, Y.F., Muller, J.P., Lewis, P., Barnsley, M., Hobson, P., Disney, M., Roberts, G., Dunderdale, M., Doll, C., d'Entremont, R.P., Hu, B.X., Liang, S.L., Privette, J.L., Roy, D., 2002. First operational BRDF, albedo nadir reflectance products from MODIS. Remote Sensing of Environment, 83, 135-148.

Schaaf, C.B., Liu, J., Gao, F., Strahler, A.H., 2011. MODIS albedo and reflectance anisotropy products from Aqua and Terra. Land Remote Sensing and Global Environmental Change: NASA's Earth Observing System and the Science of ASTER and MODIS, 11, 549-561.

Schwartz, N.B., Budsock, A.M., Uriarte, M., 2019. Fragmentation, forest structure, and topography modulate impacts of drought in a tropical forest landscape. Ecology, 100, e02677. http://doi.org/10.1002/ecy.2677.

Semmens, K.A., Anderson, M.C., Kustas, W.P., Gao, F., Alfieri, J.G., McKee, L., Prueger, J.H., Hain, C.R., Cammalleri, C., Yang, Y., Xia, T., Sanchez, L., Alsina, M.M., Velez, M., 2016. Monitoring daily evapotranspiration over two California vineyards using Landsat 8 in a multi-sensor data fusion approach. Remote Sensing of Environment, 185, 155-170.

Shendryk, Y., Rist, Y., Ticehurst, C., Thorburn, P., 2019. Deep learning for multi-modal classification of cloud, shadow and land cover scenes in PlanetScope and Sentinel-2 imagery. ISPRS Journal of Photogrammetry and Remote Sensing, 157, 124-136.

Thackeray, S.J., Henrys, P.A., Hemming, D., Bell, J.R., Botham, M.S., Burthe, S., Helaouet, P., Johns, D.G., Jones, I.D., Leech, D.I., Mackay, E.B., Massimino, D., Atkinson, S., Bacon, P.J., Brereton, T.M., Carvalho, L., Clutton-Brock, T.H., Duck, C., Edwards, M., Elliott, J.M., Hall, S.J.G., Harrington, R., Pearce-Higgins, J.W., Hoye, T.T., Kruuk, L.E.B., Pemberton, J.M., Sparks, T.H., Thompson, P.M., White, I., Winfield, I.J., Wanless, S., 2016. Phenological sensitivity to climate across taxa and trophic levels. Nature, 535, 241-245.

Viennois, G., Barbier, N., Fabre, I., Couteron, P., 2013. Multiresolution quantification of deciduousness in West-Central African forests. Biogeosciences, 10, 6957-6967.

Vrieling, A., Skidmore, A.K., Wang, T.J., Meroni, M., Ens, B.J., Oosterbeek, K., O'Connor, B., Darvishzadeh, R., Heurich, M., Shepherd, A., & Paganini, M., 2017. Spatially detailed retrievals of spring phenology from single-season high-resolution image time series. International Journal of Applied Earth Observation and Geoinformation, 59, 19-30.

Wagner, F.H., Herault, B., Bonal, D., Stahl, C., Anderson, L.O., Baker, T.R., Becker, G.S., Beeckman, H., Souza, D.B., Botosso, P.C., Bowman, D.M.J.S., Brauning, A., Brede, B., Brown, F.I., Camarero, J.J., Camargo, P.B., Cardoso, F.C.G., Carvalho, F.A., Castro, W., Chagas, R.K., Chave, J., Chidumayo, E.N., Clark, D.A., Costa, F.R.C., Couralet, C., Mauricio, P.H.D., Dalitz, H., de Castro, V.R., Milani, J.E.D., de Oliveira, E.C., Arruda, L.D.S., Devineau, J.L., Drew, D.M., Dunisch, O., Durigan, G., Elifuraha, E., Fedele, M., Fedele, L.F., Figueiredo, A., Finger, C.A.G., Franco, A.C., Freitas, J.L., Galvao, F., Gebrekirstos, A., Gliniars, R., Graca, P.M.L.D., Griffiths, A.D., Grogan, J., Guan, K., Homeier, J., Kanieski, M.R., Kho, L.K., Koenig, J., Kohler, S.V., Krepkowski, J., Lemos, J.P., Lieberman, D., Lieberman, M.E., Lisi, C.S., Santos, T.L., Ayala, J.L.L., Maeda, E.E., Malhi, Y., Maria, V.R.B., Marques, M.C.M., Marques, R., Chamba, H.M., Mbwambo, L., Melgaco, K.L.L., Mendivelso, H.A., Murphy, B.P., O'Brien, J.J., Oberbauer, S.F., Okada, N., Pelissier, R., Prior, L.D., Roig, F.A., Ross, M., Rossatto, D.R., Rossi, V., Rowland, L., Rutishauser, E., Santana, H., Schulze, M., Selhorst, D., Silva, W.R., Silveira, M., Spannl, S., Swaine, M.D., Toledo, J.J., Toledo, M.M., Toledo, M., Toma, T., Tomazello, M., Hernandez, J.I.V., Verbesselt, J., Vieira, S.A., Vincent, G., de Castilho, C.V., Volland, F., Worbes, M., Zanon, M.L.B., Aragao, L.E.O.C., 2016. Climate seasonality limits leaf carbon assimilation and wood productivity in tropical forests. Biogeosciences, 13, 2537-2562.

Walker, J.J., de Beurs, K.M., Wynne, R.H., Gao, F., 2012. Evaluation of Landsat and MODIS data fusion products for analysis of dryland forest phenology. Remote Sensing of Environment, 117, 381-393.

Wanner, W., Li, X., Strahler, A. H., 1995. On the derivation of kernels for kernel - driven models of bidirectional reflectance. Journal of Geophysical Research: Atmospheres, 100, 21077-21089.

White, M.A., de Beurs, K.M., Didan, K., Inouye, D.W., Richardson, A.D., Jensen, O.P., O'Keefe, J., Zhang, G., Nemani, R.R., van Leeuwen, W.J.D., Brown, J.F., de Wit, A., Schaepman, M., Lin, X.M., Dettinger, M., Bailey, A.S., Kimball, J., Schwartz, M.D., Baldocchi, D.D., Lee, J.T., Lauenroth, W.K., 2009. Intercomparison, interpretation, and assessment of spring phenology in North America estimated from remote sensing for 1982-2006. Global Change Biology, 15, 2335-2359.

Wright, J.S., Fu, R., Worden, J. R., Chakraborty, S., Clinton, N. E., Risi, C., Sun, Y., Yin, L., 2017. Rainforest-initiated wet season onset over the southern Amazon. Proceedings of the National Academy of Sciences, 114, 8481-8486.

Wu, J., Albert, L.P., Lopes, A.P., Restrepo-Coupe, N., Hayek, M., Wiedemann, K.T., Guan, K.Y., Stark, S.C., Christoffersen, B., Prohaska, N., Tavares, J.V., Marostica, S., Kobayashi, H., Ferreira, M.L., Campos, K.S., da Silva, R., Brando, P.M., Dye, D.G., Huxman, T.E., Huete, A.R., Nelson, B.W., Saleska, S.R., 2016. Leaf development and demography explain photosynthetic seasonality in Amazon evergreen forests. Science, 351, 972-976.

Wu, J., Kobayashi, H., Stark, S.C., Meng, R., Guan, K.Y., Tran, N.N., Gao, S.C., Yang, W., Restrepo-Coupe, N., Miura, T., Oliviera, R.C., Rogers, A., Dye, D.G., Nelson, B.W., Serbin, S.P., Huete, A.R., Saleska, S.R., 2018. Biological processes dominate seasonality of remotely sensed canopy greenness in an Amazon evergreen forest. New Phytologist, 217, 1507-1520.

Wu, S.B., Wen, J.G., Gastellu-Etchegorry, J.P., Liu, Q.H., You, D.Q., Xiao, Q., Hao, D.L., Lin, X.W., Yin, T.G., 2019a. The definition of remotely sensed reflectance quantities suitable for rugged terrain. Remote Sensing of Environment, 225, 403-415.

Wu, S.B., Wen, J.G., Lin, X.W., Hao, D.L., You, D.Q., Xiao, Q., Liu, Q.H., Yin, T.G., 2019b. Modeling discrete forest anisotropic reflectance over a sloped surface with an extended GOMS and SAIL model. IEEE Transactions on Geoscience and Remote Sensing, 57, 944-957.

Xu, X.T., Medvigy, D., Powers, J.S., Becknell, J.M., Guan, K.Y., 2016. Diversity in plant hydraulic traits explains seasonal and inter-annual variations of vegetation dynamics in seasonally dry tropical forests. New Phytologist, 212, 80-95.

Xu, X.T., Medvigy, D., Wright, S.J., Kitajima, K., Wu, J., Albert, L.P., Martins, G.A., Saleska, S.R., Pacala, S.W., 2017. Variations of leaf longevity in tropical moist forests predicted by a trait-driven carbon optimality model. Ecology Letters, 20, 1097-1106.

Yang, X.J., Lo, C.P., 2000. Relative radiometric normalization performance for change detection from multi-date satellite images. Photogrammetric Engineering and Remote Sensing, 66, 967-980.

Yang, Y., Anderson, M.C., Gao, F., Hain, C.R., Semmens, K.A., Kustas, W.P., Noormets, A., Wynne, R.H., Thomas, V.A., Sun, G., 2017. Daily Landsat-scale evapotranspiration estimation over a forested landscape in North Carolina, USA, using multi-satellite data fusion. Hydrology and Earth System Sciences, 21, 1017-1037.

Zeng, Z.Z., Estes, L., Ziegler, A.D., Chen, A.P., Searchinger, T., Hua, F.Y., Guan, K.Y., Jintrawet, A., Wood, E.F., 2018. Highland cropland expansion and forest loss in Southeast Asia in the twenty-first century. Nature Geoscience, 11, 556-562.

Tables and Figure captions

Table 1. Spatial resolutions, accessed data time ranges, and spectral bands and band-specific wavelength ranges of PlanetScope and MODIS data used at the k67 site.

Satellite	Spatial resolution (m)	Accessed data time range	Spectral band and wavelength range (nm)			
			Blue	Green	Red	NIR
PlanetScope	3	06/2018-11/2018 06/2019-11/2019	455-515	500-590	590-670	780-860
MODIS	500	02/2000-12/2019	459-479	545-565	620-670	841-876

Figure captions

Figure 1. Locations and multi-scale observations at the k67 tower site and Alter do Chão site in a Central Amazon evergreen forest in Brazil. (a) The locations of the study sites, including the red pentagram for the k67 site and green square for the Alter do Chão site; and the multi-scale observations include (b) tower-mounted phenocam (temporal coverage: 2010-2011; spatial coverage: about 200m×300m) at the k67 site, which was equipped with a 3-band (NIR, red, and green) Tetracam Agricultural Digital Camera, and thus green vegetation in the camera image (false red composited by RGB=NIR-red-green) looks red; (c) PlanetScope data of near daily nadir coverage at a 3m spatial resolution at the k67 site (temporal coverage: dry season of 2018 and 2019; spatial coverage: 10km×10km); (d) daily MODIS data of a 500m spatial resolution at the k67 site (temporal coverage: 2000-2019; spatial coverage: 10km×10km); (e) PlanetScope data at the Alter do Chão site (temporal coverage: dry season of 2018; spatial coverage: 8km×8km); and (f) MODIS data at the Alter do Chão site (temporal coverage: 2000-2019; spatial coverage: 8km×8km). The background figure in panel (a) is adapted from National Geographic, ESRI; phenocam data can be accessed from Wu et al. (2016); satellite data of the two sites in panel (c)-(f) are displayed in the same false red composite as phenocam; the k67 site is used to evaluate the multi-scale approach for tropical phenology monitoring, and the Alter do Chão site is used to evaluate robustness of the approach.

Figure 2. Flowchart of the method. It includes four major tasks: 1) acquiring and processing the PlanetScope and MODIS data, 2) cross-calibrating the PlanetScope data using BRDF-adjusted MODIS, 3) extracting reflectance spectra of the three key endmembers comprising tropical forest canopies and estimating the fractions of non-photosynthetic vegetation (NPV) and green vegetation (GV) of each pixel in the calibrated PlanetScope images, and 4) evaluating the accuracy of PlanetScope-derived seasonal trends in NPV and GV fractions by comparing with ground-based measurements of leaf phenology.

Figure 3. Example demonstration of band-specific outlier detection and gap-filling for BRDF-adjusted MODIS seasonality in 2018, including reflectance bands of (a) blue, (b) green, (c) red, and (d) NIR. The 20-year (i.e. 2000-2019) mean MODIS seasonality is displayed with the mean values in black lines, and grey shading for 95% confidence interval (i.e. 2.5 percentile for bottom and 97.5 percentile for top); the 2018 seasonality after quality control is displayed with valid data points (blue crosses, within the 95% confidence interval of 20-year mean seasonality) and outlier data points (blue circles, outside the 95% confidence interval); the gap-filling results in 2018 are displayed as red lines for daily means and red shadings for 95% confidence interval. A 5km×5km area centered on the k67 tower site is used here for demonstration purposes. Light grey shading indicates the dry season of the k67 site.

Figure 4. Example demonstration of band-specific histograms and the fitted Gaussian distribution curves for BRDF-adjusted MODIS (shown as red) and upscaled PlanetScope (shown as green) on November 21, 2018, including reflectance bands of (a) blue, (b) green, (c) red, and (d) NIR. The spatial extent used here includes a 10km×10km area centered on the k67 tower site. BRDF-adjusted MODIS has a spatial resolution of 500m; upscaled PlanetScope refers to upscaling the original PlanetScope of a 3m spatial resolution to the same spatial resolution as that of MODIS;

the probability distribution function (PDF) is used to describe the fitted Gaussian distribution curves.

Figure 5. Ecosystem-scale seasonality of BRDF-adjusted MODIS (20-year mean in black and its 95% confidence interval in grey shading, and 2018 gap-filled in red) and 2018 PlanetScope (uncalibrated in blue and calibrated in green), including reflectance bands of (a) blue, (b) green, (c) red, and (d) NIR, and vegetation indices of (e) Normalized Difference Vegetation Index (NDVI), and (f) Enhanced Vegetation Index (EVI). BRDF-adjusted MODIS including both 20-year mean and 2018 gap-filled are displayed as background information; the uncalibrated/calibrated PlanetScope is based on the histogram matching analysis as shown in Fig. 4; and a 3km×3km area centered on the k67 tower site is used here to calculate ecosystem-scale seasonality. Light grey shading indicates the dry season of the k67 site.

Figure 6. Seasonal variation in PlanetScope-derived reflectance spectra of stable permanent objects (urban buildings) (a) prior and (b) post cross-calibration. The 180 building pixels were carefully and manually extracted from an area of 8km×8km centered on the town of Alter do Chão, Brazil, which is 37 km from the k67 tower site (see Fig. 1 for more details). Error bars indicate one standard deviation for the reflectance spectra among all building pixels; each colored line indicates one of nine selected dates of PlanetScope measurements in 2018; these selected dates cover the full dry season at the k67 site and the Alter do Chão site.

Figure 7. The extracted mean (color lines) and one standard deviation (error bars) of reflectance spectra for three key endmembers at the k67 site using all the calibrated PlanetScope data from June to November in 2018 and 2019. These three endmembers are pixels of completely leafless tree-crowns for pure non-photosynthetic vegetation (NPV), leafy tree-crowns for pure green vegetation (GV), and deep shade/shadow portions of the canopy (shade).

Figure 8. Spatial and temporal variations in canopy reflectance for calibrated PlanetScope (top panel) and corresponding magnified PlanetScope (bottom panel) (composited as RGB=NIR-red-blue). For demonstration purposes, we selected 6 dates among all 22 dates of PlanetScope measurements during the dry season of 2018, including one date per month from June to November (i.e. June 15, July 06, August 20, September 20, October 15, and November 01 from left to right); each image subset (shown in top panel) centered on the k67 tower site has a spatial coverage of 500m×500m (=one MODIS pixel).

Figure 9. Comparisons of PlanetScope-derived phenology metrics and ground-based phenology measurements, including a) PlanetScope-derived and tower-phenocam measurements of NPV fraction, and b) PlanetScope-derived and tower-phenocam measurements of GV fraction and field LAI measurements. The calibrated PlanetScope data in 2018 are used here, and the PlanetScope-derived phenology metrics represent an average of a 3km×3km area centered on the k67 site; error bars indicate one standard deviation. Tower-phenocam measurements in 2010-2011 (conducted in an about 200m×300m area centered on the k67 site) and field LAI measurements in 2000-2005 (a 100m×100m plot, ~5 km apart from the k67 site) are based on the literature values (Brando et al., 2010; Wu et al., 2016; see methods for details).

Figure 10. Spatial and temporal variations in PlanetScope-derived NPV fraction in an area of 500m×500m centered on the k67 tower site (top panel) and in eight pixels located in the same area (bottom panel). The spatial extent shown in the top panel is the same as Fig. 8, and 6 dates among a total of 22 dates in the dry season of 2018 are selected, including one date per month from June to November (June 15, July 06, August 20, September 20, October 15, and November 01 from left to right). The gray bar with a range from 0 to 1 represents an increasing NPV fraction from 0 to 100% within an image pixel. For demonstration purposes, spatial and temporal dynamics of NPV fraction in eight pixels (A to H) are shown in the bottom panel, with the ecosystem-scale average NPV fraction of a 3km×3km area centered on the k67 site shown in black line; error bars indicate one standard deviation.

Figure 11. Assessing the dry-season change rate in NPV fraction derived from the calibrated PlanetScope data in 2018, including (a) a map of dry-season change rate in NPV fraction for an area of 500m×500m centered on the k67 tower site (the same as Fig. 10), and (b) statistical summary on frequency distribution of dry-season change rate for all pixels shown in panel (a). The dry-season change rate in NPV fraction is assessed through a linear regression analysis between dry-season change in NPV fraction and day of year in the dry season. The dry-season change rate in NPV fraction has a range from -0.005 to 0.005, with a negative value indicating dry-season decrease in NPV fraction (or green-up) and a positive value rate indicating dry-season increase in NPV fraction (or brown-down). In this area, there are 84.6% of pixels showing a dry-season green-up trend and 15.4% showing a brown-down trend.

Figure
Click here to download Figure: FiguresR2_v7.6.pdf

Figures and Tables

Figure 1. Locations and multi-scale observations at the k67 tower site and Alter do Chão site in a Central Amazon evergreen forest in Brazil. (a) The locations of the study sites, including the red pentagram for the k67 site and green square for the Alter do Chão site; and the multi-scale observations include (b) tower-mounted phenocam (temporal coverage: 2010-2011; spatial coverage: about 200m×300m) at the k67 site, which was equipped with a 3-band (NIR, red, and green) Tetracam Agricultural Digital Camera, and thus green vegetation in the camera image (false red composited by RGB=NIR-red-green) looks red; (c) PlanetScope data of near daily nadir coverage at a 3m spatial resolution at the k67 site (temporal coverage: dry season of 2018 and 2019; spatial coverage: 10km×10km); (d) daily MODIS data of a 500m spatial resolution at the k67 site (temporal coverage: 2000-2019; spatial coverage: 10km×10km); (e) PlanetScope data at the Alter do Chão site (temporal coverage: dry season of 2018; spatial coverage: 8km×8km); and (f) MODIS data at the Alter do Chão site (temporal coverage: 2000-2019; spatial coverage: 8km×8km). The background figure in panel (a) is adapted from National Geographic, ESRI; phenocam data can be accessed from Wu et al. (2016); satellite data of the two sites in panel (c)-(f) are displayed in the same false red composite as phenocam; the k67 site is used to evaluate the multi-scale approach for tropical phenology monitoring, and the Alter do Chão site is used to evaluate robustness of the approach.

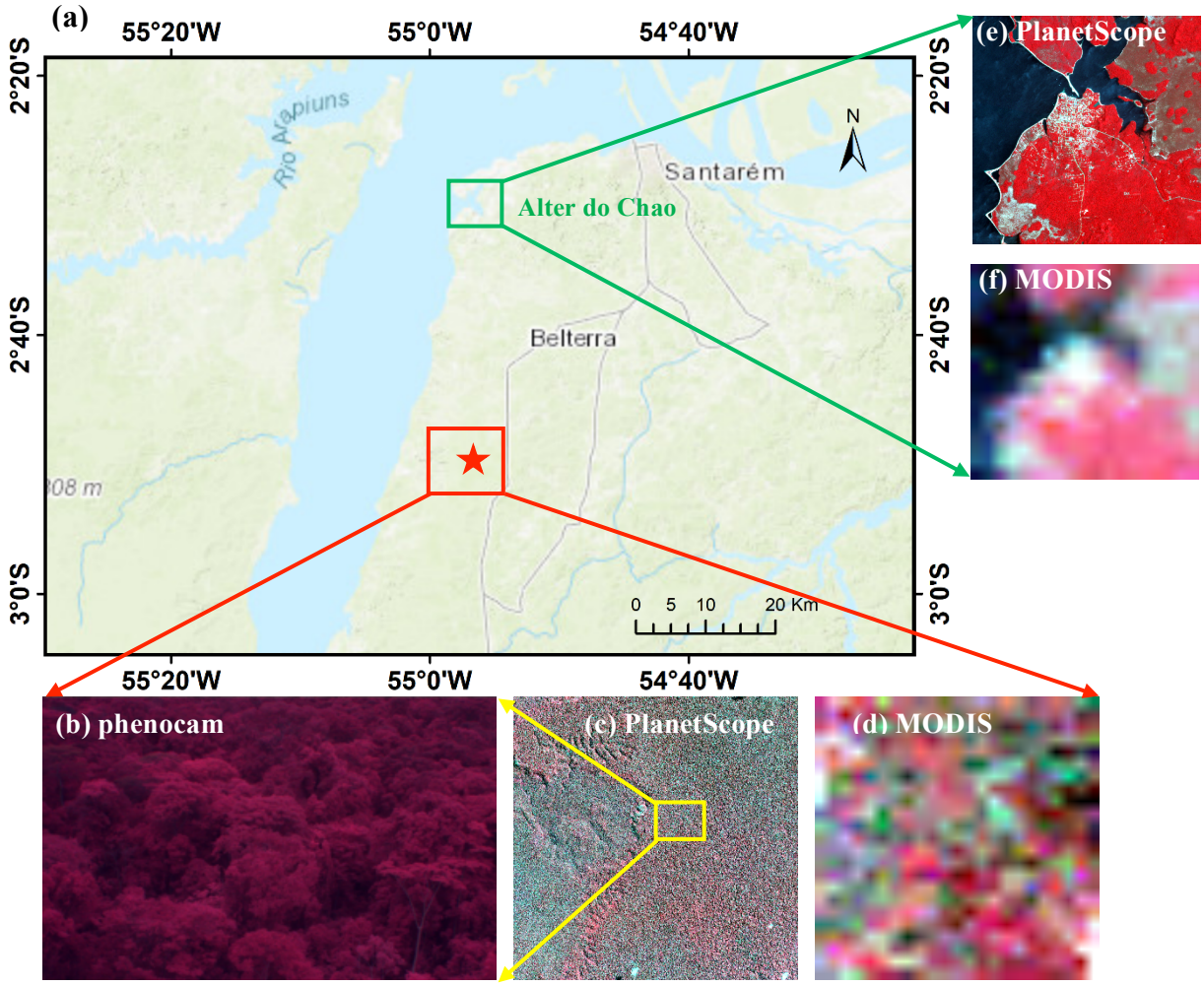

Figure 2. Flowchart of the method. It includes four major tasks: 1) acquiring and processing the PlanetScope and MODIS data, 2) cross-calibrating the PlanetScope data using BRDF-adjusted MODIS, 3) extracting reflectance spectra of the three key endmembers comprising tropical forest canopies and estimating the fractions of non-photosynthetic vegetation (NPV) and green vegetation (GV) of each pixel in the calibrated PlanetScope images, and 4) evaluating the accuracy of PlanetScope-derived seasonal trends in NPV and GV fractions by comparing with ground-based measurements of leaf phenology.

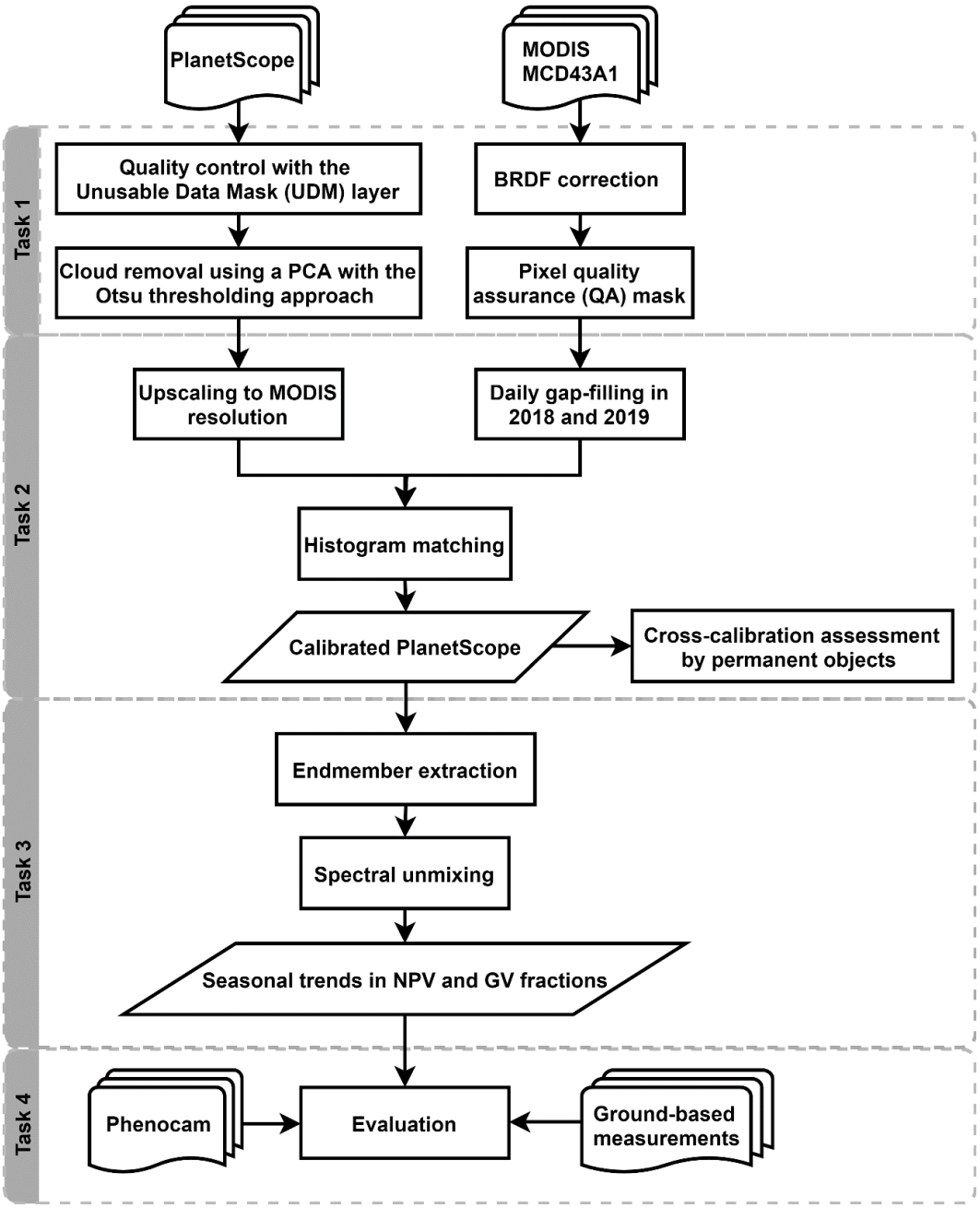

Figure 3. Example demonstration of band-specific outlier detection and gap-filling for BRDF-adjusted MODIS seasonality in 2018, including reflectance bands of (a) blue, (b) green, (c) red, and (d) NIR. The 20-year (i.e. 2000-2019) mean MODIS seasonality is displayed with the mean values in black lines, and grey shading for 95% confidence interval (i.e. 2.5 percentile for bottom and 97.5 percentile for top); the 2018 seasonality after quality control is displayed with valid data points (blue crosses, within the 95% confidence interval of 20-year mean seasonality) and outlier data points (blue circles, outside the 95% confidence interval); the gap-filling results in 2018 are displayed as red lines for daily means and red shadings for 95% confidence interval. A 5km×5km area centered on the k67 tower site is used here for demonstration purposes. Light grey shading indicates the dry season of the k67 site.

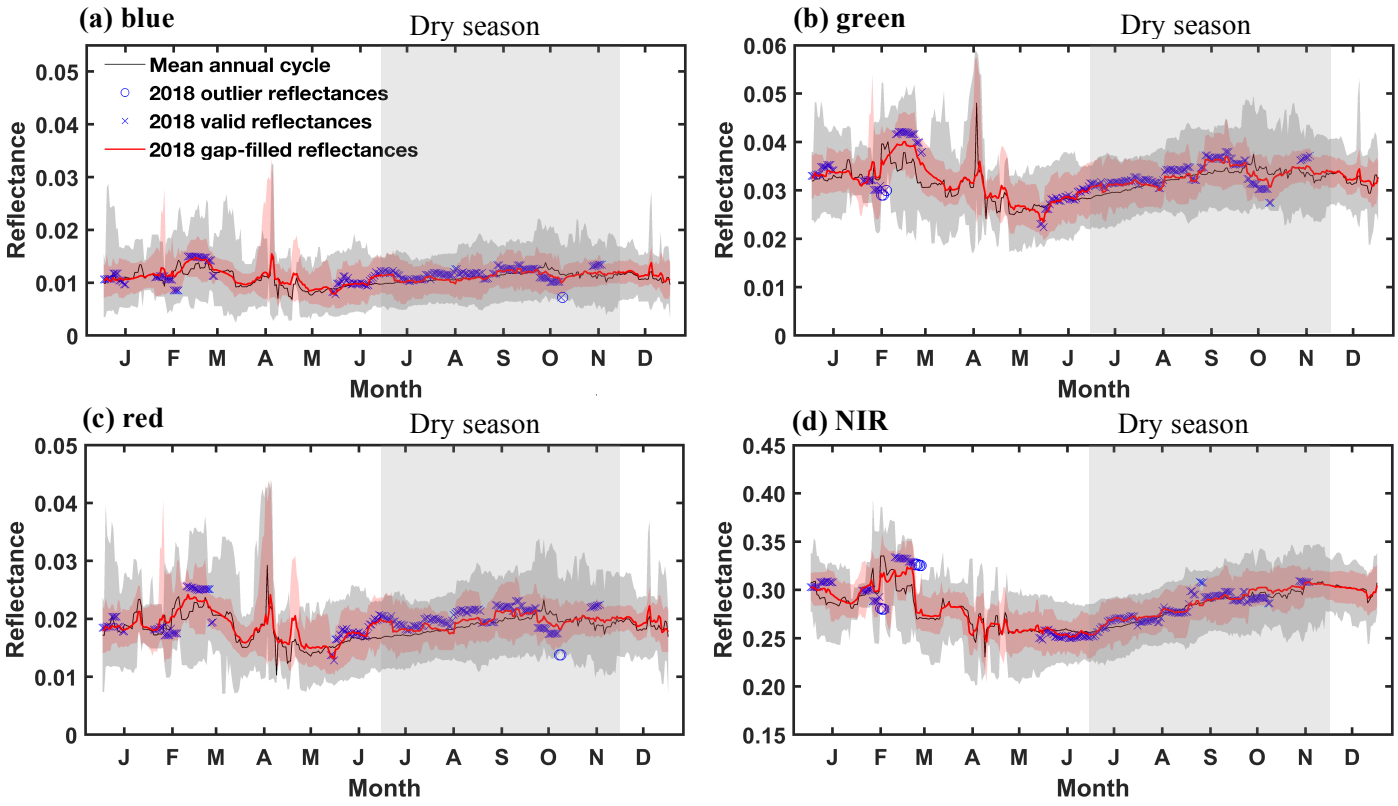

Figure 4. Example demonstration of band-specific histograms and the fitted Gaussian distribution curves for BRDF-adjusted MODIS (shown as red) and upscaled PlanetScope (shown as green) on November 21, 2018, including reflectance bands of (a) blue, (b) green, (c) red, and (d) NIR. The spatial extent used here includes a 10km×10km area centered on the k67 tower site. BRDF-adjusted MODIS has a spatial resolution of 500m; upscaled PlanetScope refers to upscaling the original PlanetScope of a 3m spatial resolution to the same spatial resolution as that of MODIS; the probability distribution function (PDF) is used to describe the fitted Gaussian distribution curves.

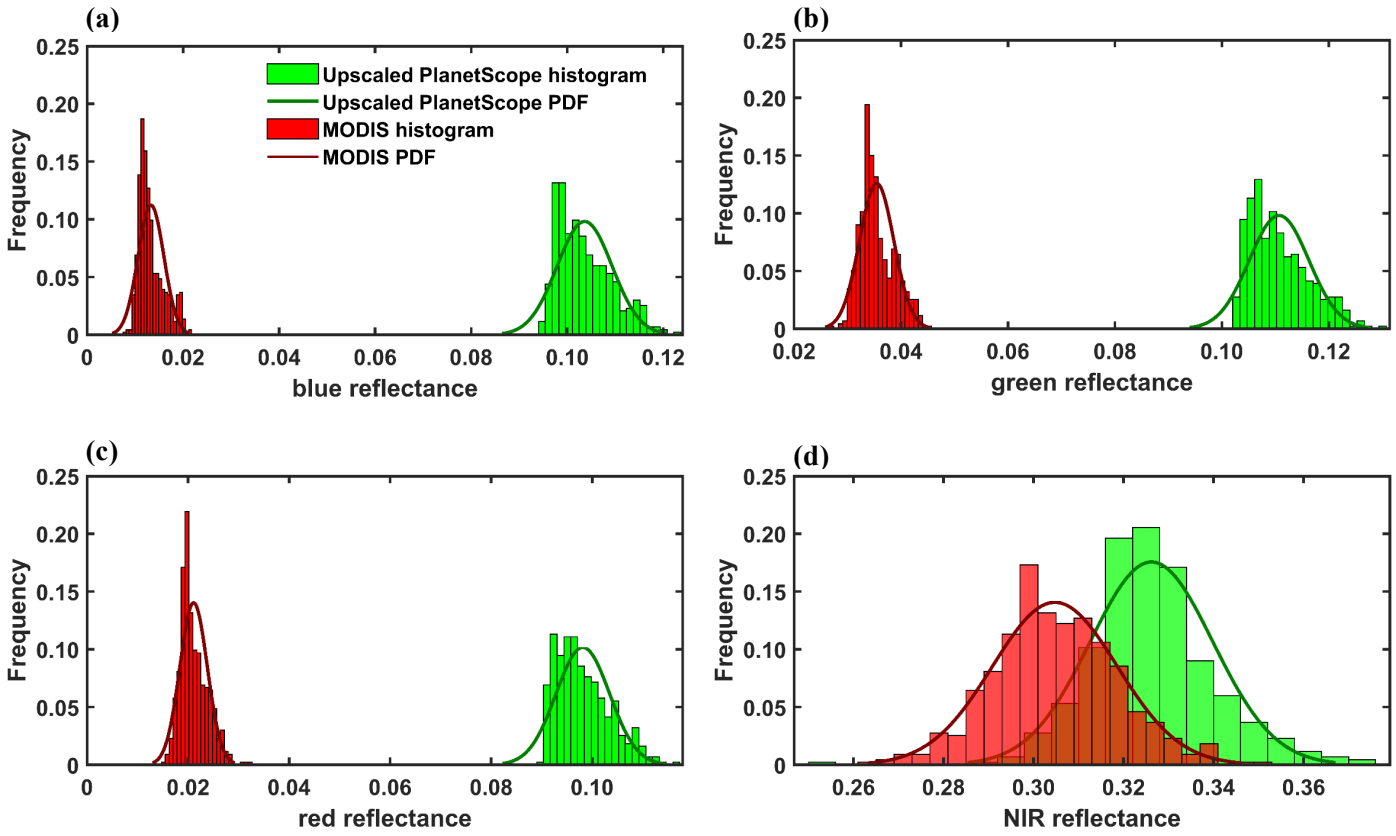

Figure 5. Ecosystem-scale seasonality of BRDF-adjusted MODIS (20-year mean in black and its 95% confidence interval in grey shading, and 2018 gap-filled in red) and 2018 PlanetScope (uncalibrated in blue and calibrated in green), including reflectance bands of (a) blue, (b) green, (c) red, and (d) NIR, and vegetation indices of (e) Normalized Difference Vegetation Index (NDVI), and (f) Enhanced Vegetation Index (EVI). BRDF-adjusted MODIS including both 20-year mean and 2018 gap-filled are displayed as background information; the uncalibrated/calibrated PlanetScope is based on the histogram matching analysis as shown in Fig. 4; and a 3km×3km area centered on the k67 tower site is used here to calculate ecosystem-scale seasonality. Light grey shading indicates the dry season of the k67 site.

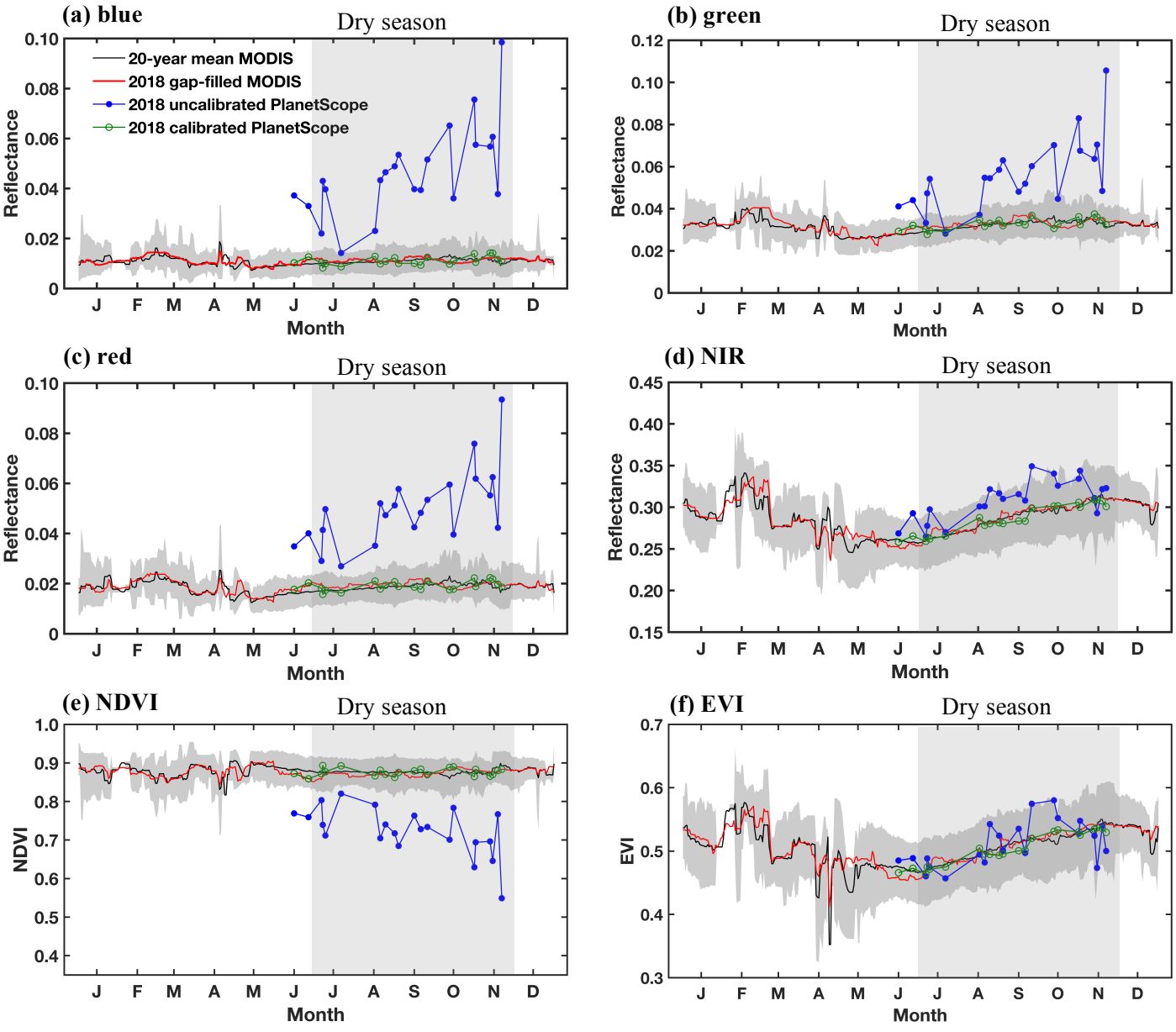

Figure 6. Seasonal variation in PlanetScope-derived reflectance spectra of stable permanent objects (urban buildings) (a) prior and (b) post cross-calibration. The 180 building pixels were carefully and manually extracted from an area of 8km×8km centered on the town of Alter do Chão, Brazil, which is 37 km from the k67 tower site (see Fig. 1 for more details). Error bars indicate one standard deviation for the reflectance spectra among all building pixels; each colored line indicates one of nine selected dates of PlanetScope measurements in 2018; these selected dates cover the full dry season at the k67 site and the Alter do Chão site.

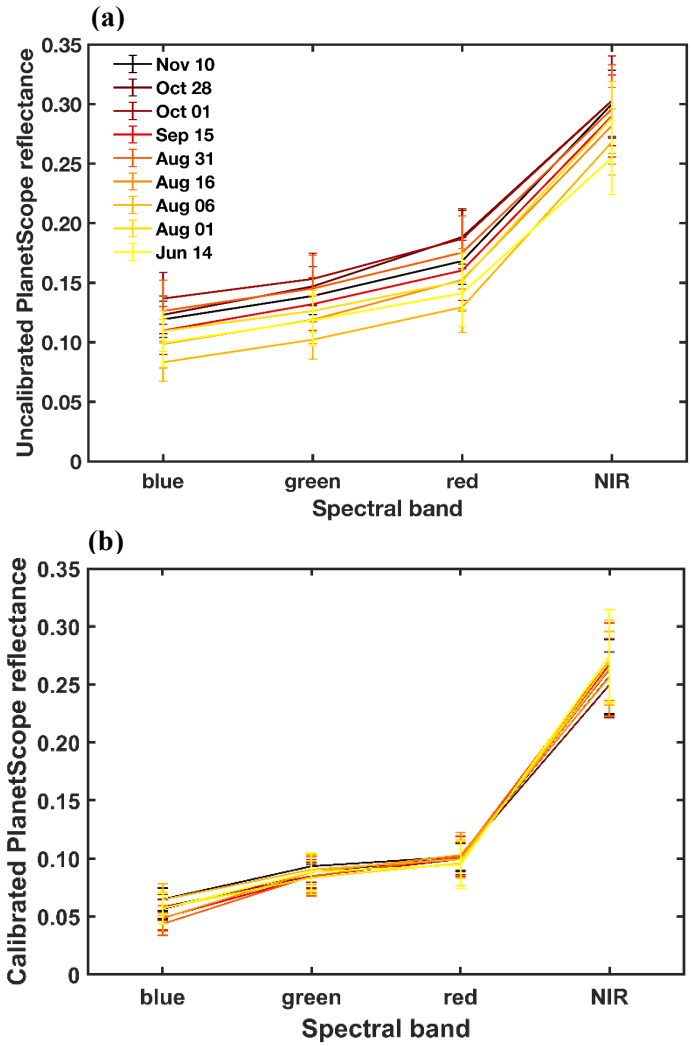

Figure 7. The extracted mean (color lines) and one standard deviation (error bars) of reflectance spectra for three key endmembers at the k67 site using all the calibrated PlanetScope data from June to November in 2018 and 2019. These three endmembers are pixels of completely leafless tree-crowns for pure non-photosynthetic vegetation (NPV), leafy tree-crowns for pure green vegetation (GV), and deep shade/shadow portions of the canopy (shade).

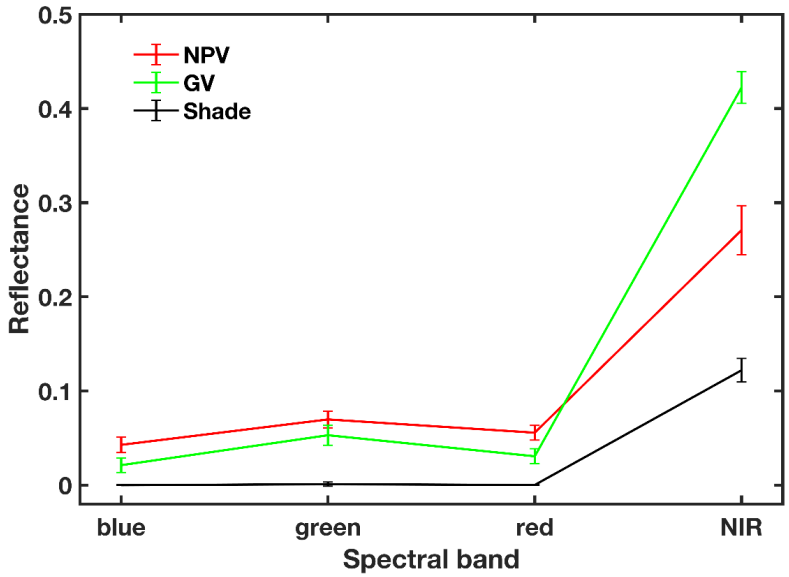

Figure 8. Spatial and temporal variations in canopy reflectance for calibrated PlanetScope (top panel) and corresponding magnified PlanetScope (bottom panel) (composited as RGB=NIR-red-blue). For demonstration purposes, we selected 6 dates among all 22 dates of PlanetScope measurements during the dry season of 2018, including one date per month from June to November (i.e. June 15, July 06, August 20, September 20, October 15, and November 01 from left to right); each image subset (shown in top panel) centered on the k67 tower site has a spatial coverage of 500m×500m (=one MODIS pixel).

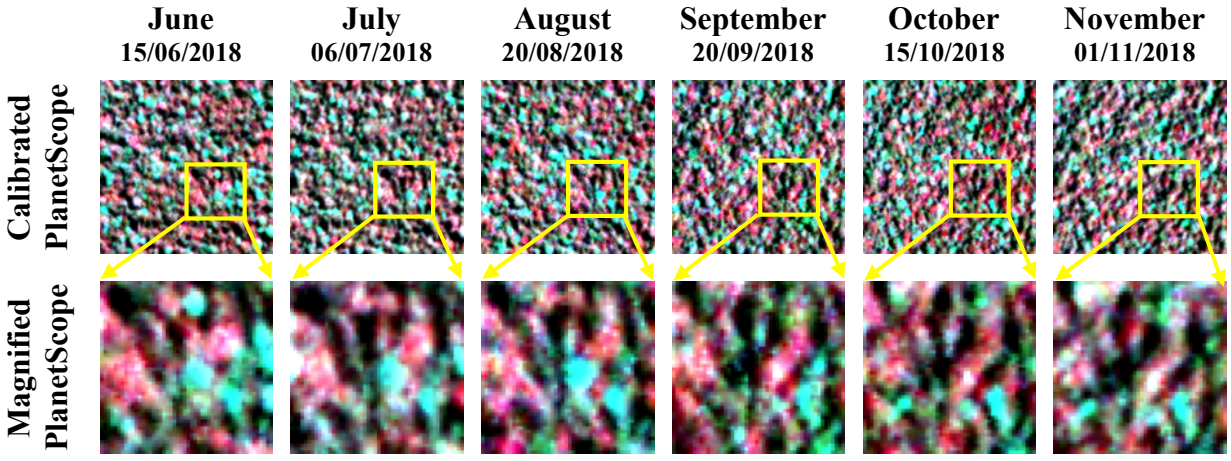

Figure 9. Comparisons of PlanetScope-derived phenology metrics and ground-based phenology measurements, including a) PlanetScope-derived and tower-phenocam measurements of NPV fraction, and b) PlanetScope-derived and tower-phenocam measurements of GV fraction and field LAI measurements. The calibrated PlanetScope data in 2018 are used here, and the PlanetScope-derived phenology metrics represent an average of a 3km×3km area centered on the k67 site; error bars indicate one standard deviation. Tower-phenocam measurements in 2010-2011 (conducted in an about 200m×300m area centered on the k67 site) and field LAI measurements in 2000-2005 (a 100m×100m plot, ~5 km apart from the k67 site) are based on the literature values (Brando et al., 2010; Wu et al., 2016; see methods for details).

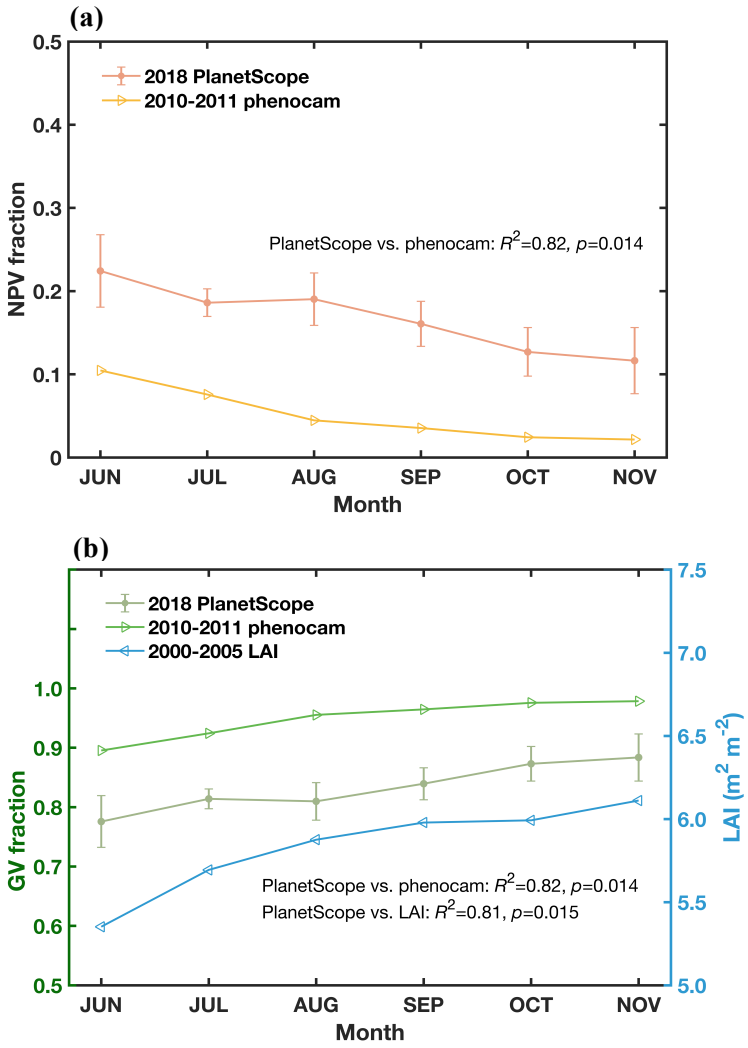

Figure 10. Spatial and temporal variations in PlanetScope-derived NPV fraction in an area of 500m×500m centered on the k67 tower site (top panel) and in eight pixels located in the same area (bottom panel). The spatial extent shown in the top panel is the same as Fig. 8, and 6 dates among a total of 22 dates in the dry season of 2018 are selected, including one date per month from June to November (June 15, July 06, August 20, September 20, October 15, and November 01 from left to right). The gray bar with a range from 0 to 1 represents an increasing NPV fraction from 0 to 100% within an image pixel. For demonstration purposes, spatial and temporal dynamics of NPV fraction in eight pixels (A to H) are shown in the bottom panel, with the ecosystem-scale average NPV fraction of a 3km×3km area centered on the k67 site shown in black line; error bars indicate one standard deviation.

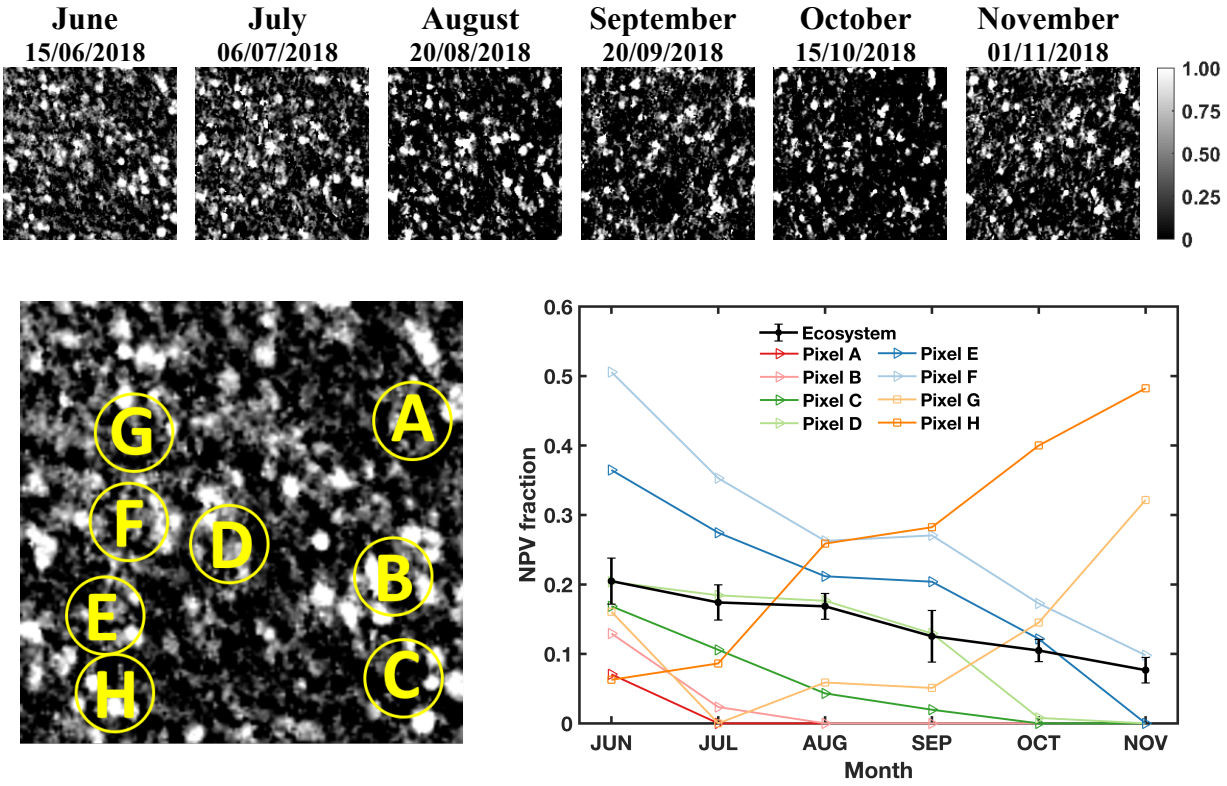

Figure 11. Assessing the dry-season change rate in NPV fraction derived from the calibrated PlanetScope data in 2018, including (a) a map of dry-season change rate in NPV fraction for an area of 500m×500m centered on the k67 tower site (the same as Fig. 10), and (b) statistical summary on frequency distribution of dry-season change rate for all pixels shown in panel (a). The dry-season change rate in NPV fraction is assessed through a linear regression analysis between dry-season change in NPV fraction and day of year in the dry season. The dry-season change rate in NPV fraction has a range from -0.005 to 0.005, with a negative value indicating dry-season decrease in NPV fraction (or green-up) and a positive value rate indicating dry-season increase in NPV fraction (or brown-down). In this area, there are 84.6% of pixels showing a dry-season green-up trend and 15.4% showing a brown-down trend.

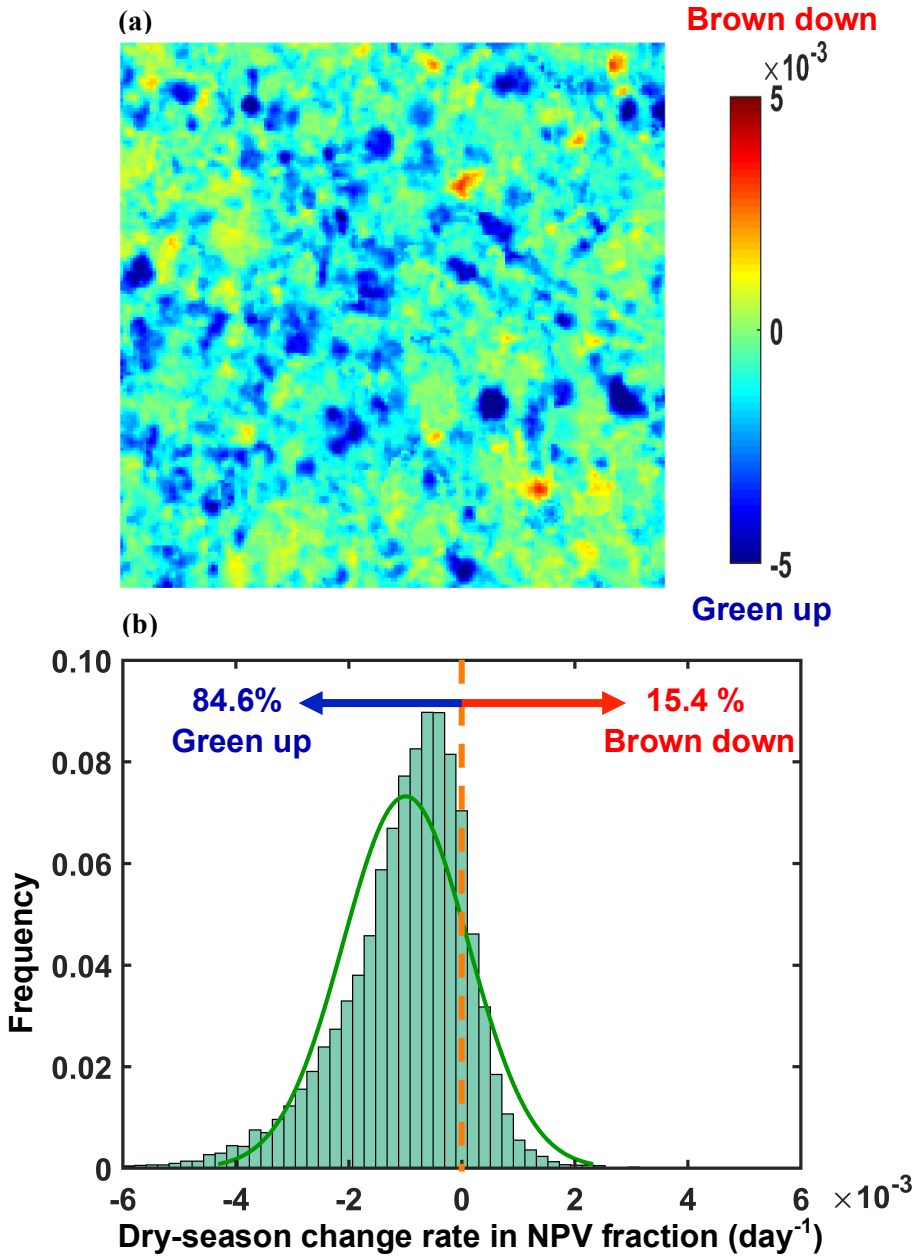

Figure S1. A true-colour RGB composited WorldView-2 image acquired at the k67 site (i.e. orange pentagram) on 28 July 2011, near-nadir view (2° off nadir). Three key endmembers, non-photosynthetic vegetation (NPV), green vegetation (GV) and shade, can be clearly identified in the image, with a few examples shown in red, light blue, and yellow, respectively. The figure is adopted from Fig. S1 in Wu et al. (2018), and for demonstration purposes, the WorldView-2 image of an area of about 1km×0.6km surrounding the k67 tower is displayed here as background.

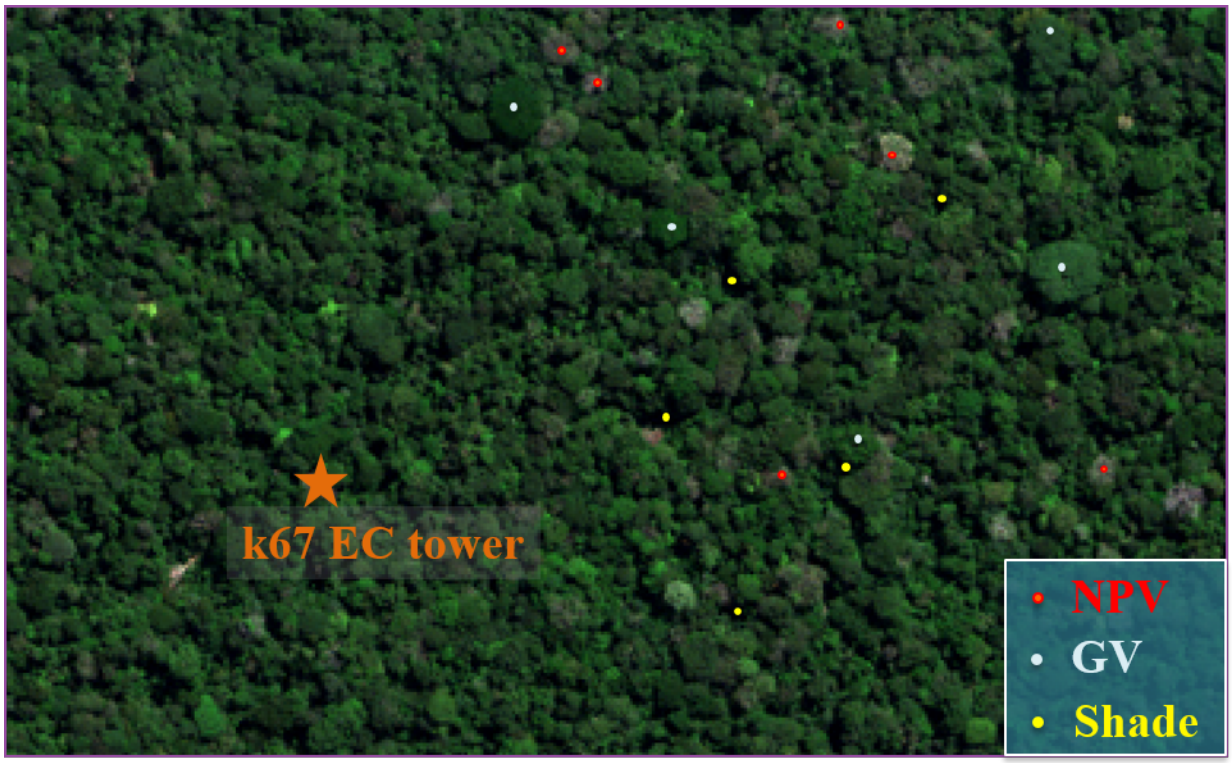

Figure S2. Color maps of the three gap-filling scenarios for each reflectance band (i.e. namely, blue, green, red and NIR) of BRDF-adjusted MODIS data at the k67 site in 2018 and 2019 and the Alter do Chão site in 2018. The color index for the following three scenarios are: for each band of a target MODIS pixel in the current year (2018/2019), it has (i) ≥ 200 valid daily measurements (blue color), (ii) ≥ 50 and <200 valid daily measurements (green color), and (iii) < 50 valid daily measurements (red color). The spatial extent of the k67 site is a 10km×10km area; the spatial extent of the Alter do Chão site is a 8km×8km area; the spatial resolution of MODIS data used is 500m. Also see more details in Section 3.2.2.

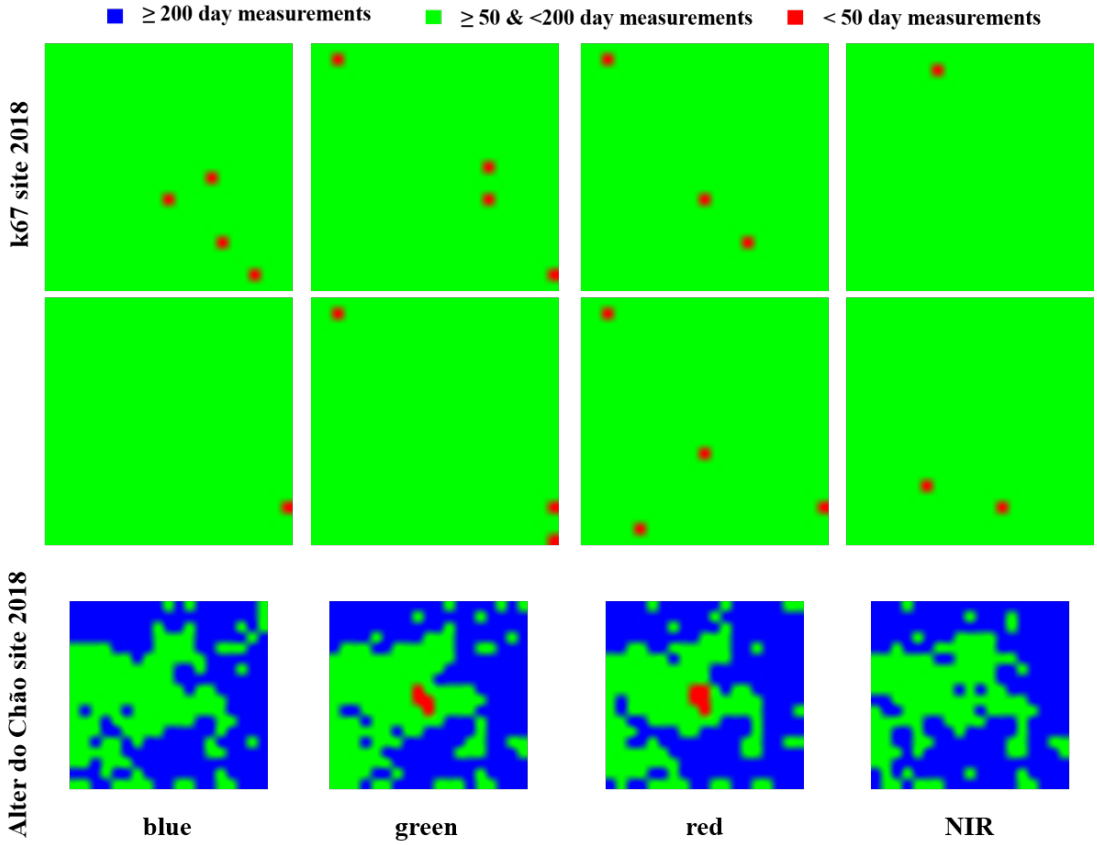

Figure S3. Example demonstration of band-specific outlier detection and gap-filling for BRDF-adjusted MODIS seasonality in 2019, including reflectance bands of (a) blue, (b) green, (c) red, and (d) NIR. The 20-year (i.e. 2000-2019) mean MODIS seasonality is displayed with the mean values in black lines, and grey shading for 95% confidence interval (i.e. 2.5 percentile for bottom and 97.5 percentile for top); the 2019 seasonality after quality control is displayed with valid data points (blue crosses, within the 95% confidence interval of 20-year mean seasonality) and outlier data points (blue circles, outside the 95% confidence interval); the gap-filling results in 2019 are displayed as red lines for daily means and red shadings for 95% confidence interval. A 5km×5km area centered on the k67 tower site is used here for demonstration purposes. Light grey shading indicates the dry season of the k67 site.

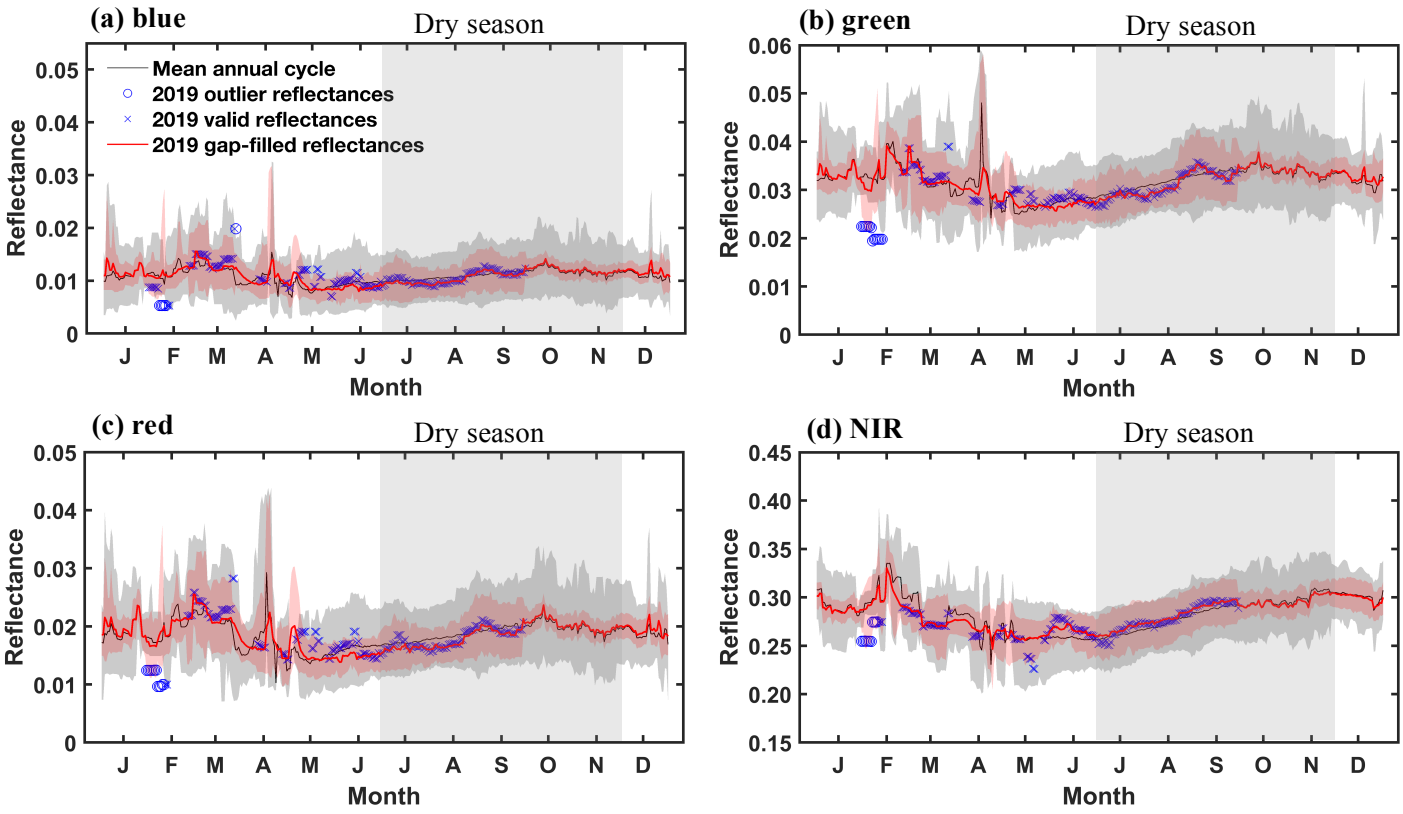

Figure S4. Evaluating the effect of gap-filling thresholds on the derived gap-filling results. Ecosystem-scale average daily MODIS reflectance of a 5km×5km area centered on the k67 tower site in 2018 is displayed here for demonstration, including reflectance bands of (a) blue, (b) green, (c) red, and (d) NIR. The original, non-gap-filled daily MODIS measurements are displayed in blue, with blue cross for valid data and blue circles for outlier data; color lines indicate five pairs of thresholds (i.e. 150 & 50; 180 & 50; 200 & 50; 200 & 80; 200 & 100) examined here, with each pair (two values) determining the cut-off of three different gap-filling scenarios. The results suggest that the seasonal trends of gap-filled MODIS in 2018 very well track that of original, non-gap-filled MODIS in 2018, and the gap-filling results are overall very stable, regardless of some variation in the thresholds used. Light grey shading indicates the dry season of the k67 site.

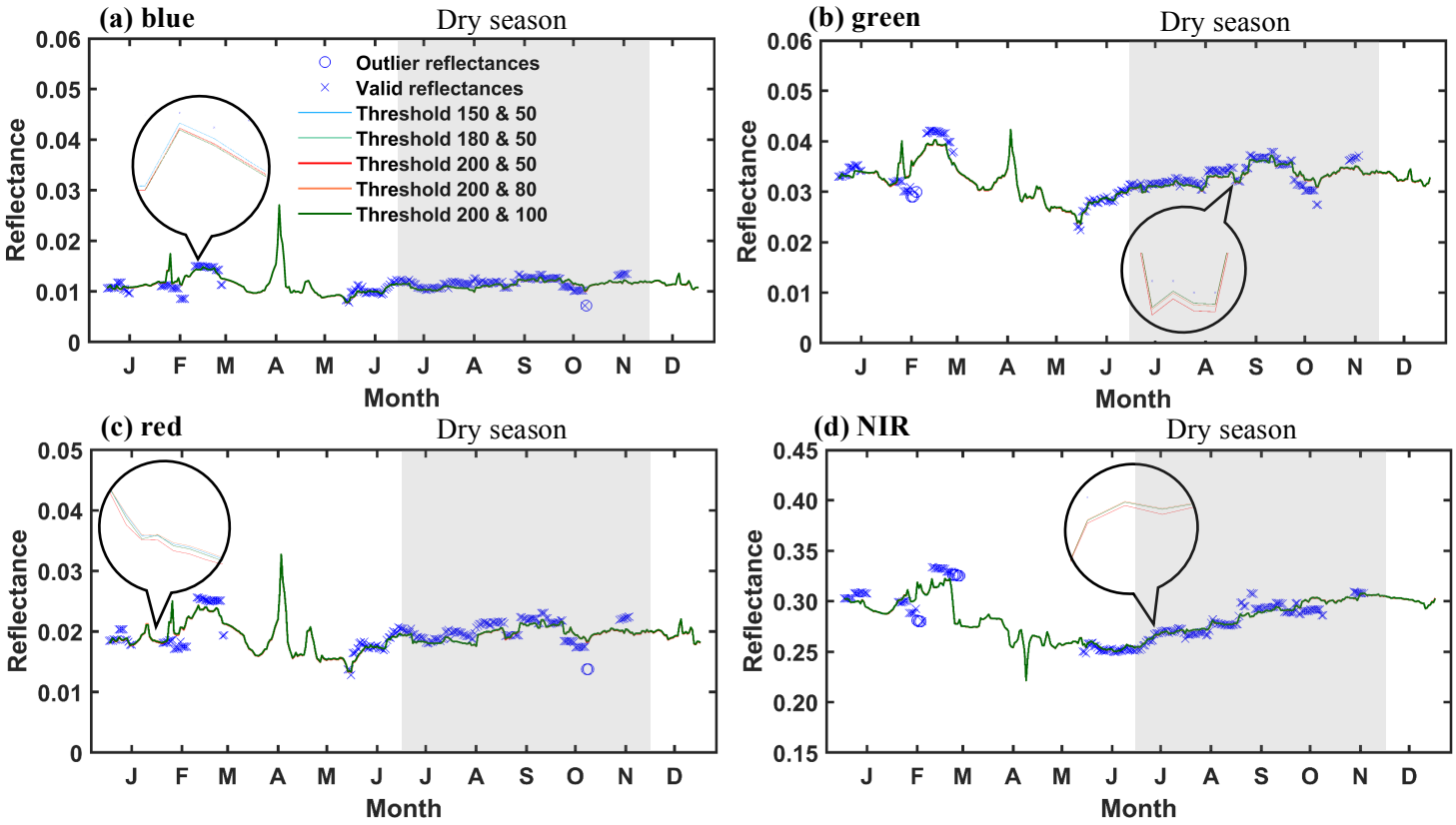

Figure S5. Comparisons of BRDF-adjusted MODIS time series in 2018 before (top panel) and after (bottom panel) gap-filling. The spatial extent shown here includes an area of 10km×10km centered on the k67 site; and the missing values (black color) represent those pixels that did not pass through the pixel quality control or suffered from the cloud/aerosol contaminations. For demonstration purposes, 6 daily MODIS images (composited by RGB=NIR-red-green bands) among a total of 183 images in the dry season of 2018 are selected, including one image per month from June to November (i.e. June 22, July 05, August 17, September 24, October 09, and November 14 from left to right).

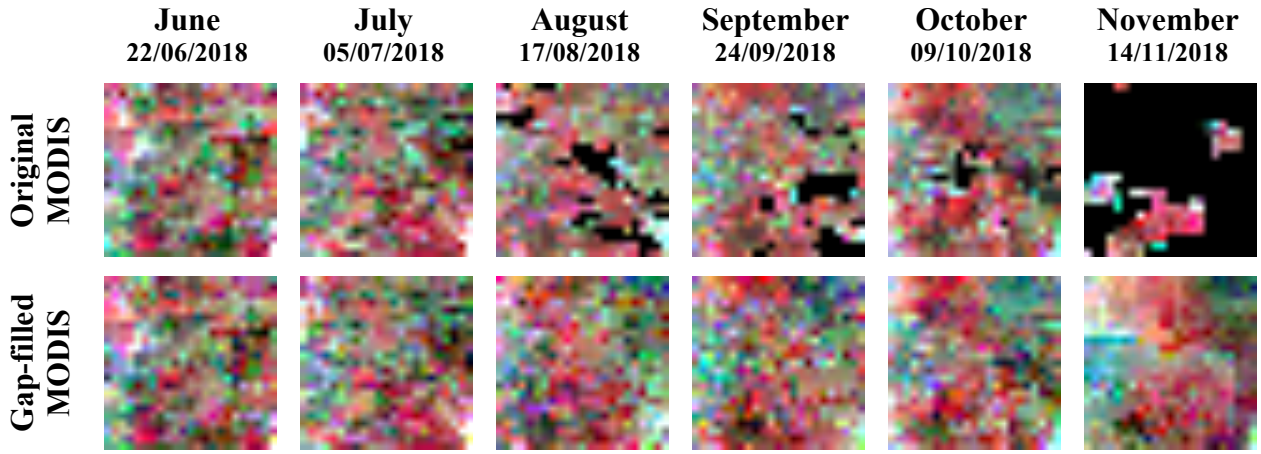

Figure S6. Comparisons of band-specific PlanetScope time series in 2018 before and after cross-calibration. Four reflectance bands (i.e. blue, green, red, and NIR) are shown here, with band-specific cross comparison indicating the difference in seasonal trend and magnitude of seasonal fluctuation between prior and post cross-calibration. The spatial extent shown here includes an area of 10km×10km centered on the k67 site; and the missing values represent those pixels that did not pass through the pixel quality control or suffered from the cloud/aerosol contaminations. For demonstration purposes, 6 dates of PlanetScope measurements among a total of 22 dates in the dry season of 2018 are selected, including one date per month from June to November (i.e. June 26, July 06, August 16, September 20, October 12, and November 14 from left to right). Color bars represent an increasing reflectance value from 0 to 0.2 (for blue, green and red bands) and 0 to 0.55 (for NIR band).

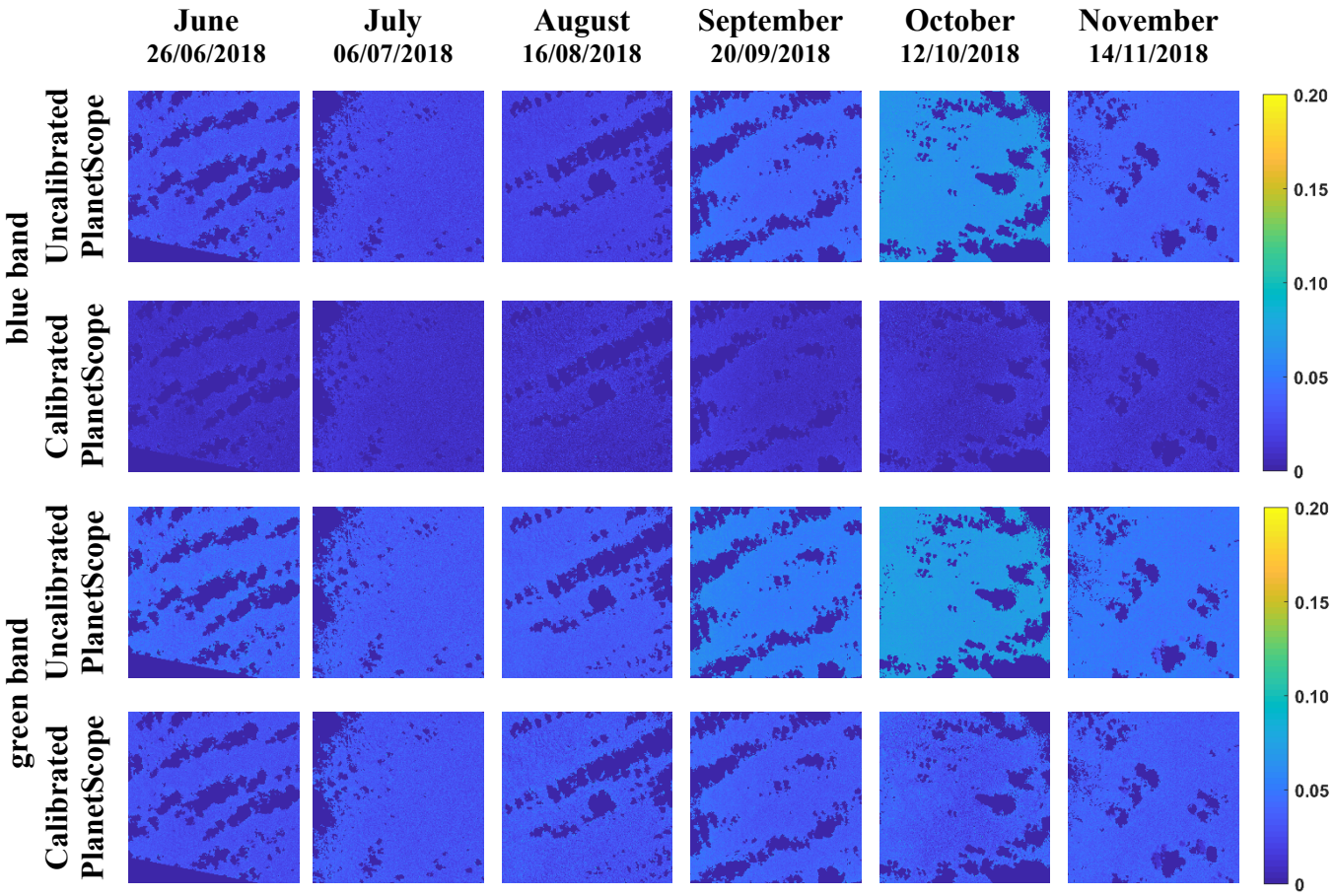

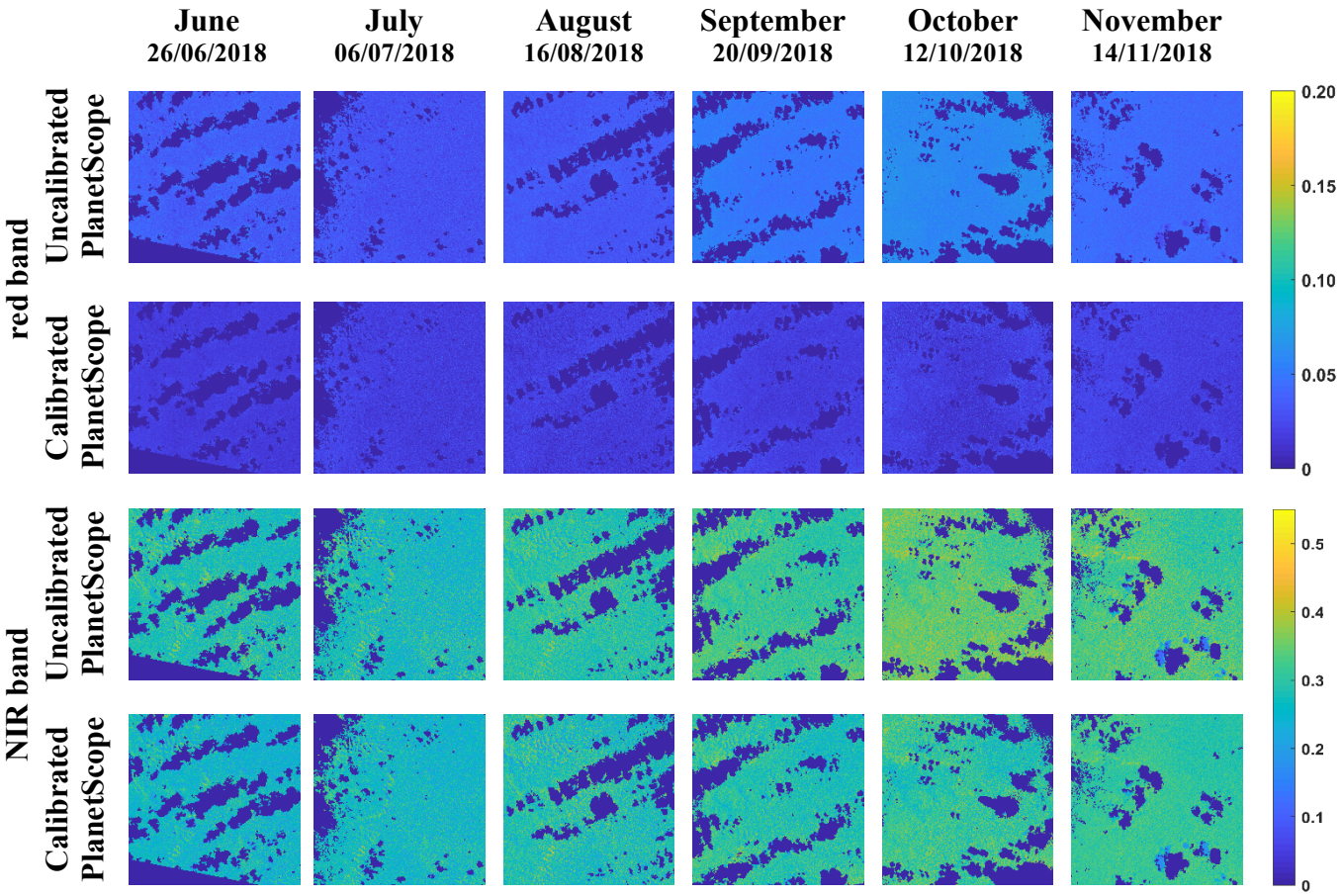
June
26/06/2018
July
06/07/2018
August
16/08/2018
September
20/09/2018
October
12/10/2018
November
14/11/2018
red band
Uncalibrated PlanetScope
Calibrated PlanetScope
NIR band
Uncalibrated PlanetScope
Calibrated PlanetScope
0.20
0.15
0.10
0.05
0
0.5
0.4
0.3
0.2
0.1
0

Figure S7. Example demonstration of endmember-specific reflectance spectra extraction, using the principle component analysis (PCA). A single PCA transformation is performed on all the calibrated PlanetScope images in 2018 and 2019 at the k67 site, and a randomly selected 1% of all image pixels of the two-dimensional feature space (i.e. the 2-D scatter plot of PC1 and PC2) is displayed in blue dots as background. The visually identified pixels of the three pure endmembers (i.e. red dots for NPV, green dots for GV, and black dots for Shade) are then overlaid on the 2-D scatter plot to aid the identification of these three key endmembers across all calibrated PlanetScope images. Further, we delimited the rectangle for each endmember, based on the mean and two standard deviations of each PCA axis derived from those manually identified pixels. Last, the average reflectance per band for all image pixels found within the three rectangles is calculated to derive endmember-specific reflectance spectra (see the results shown in Fig. 7).

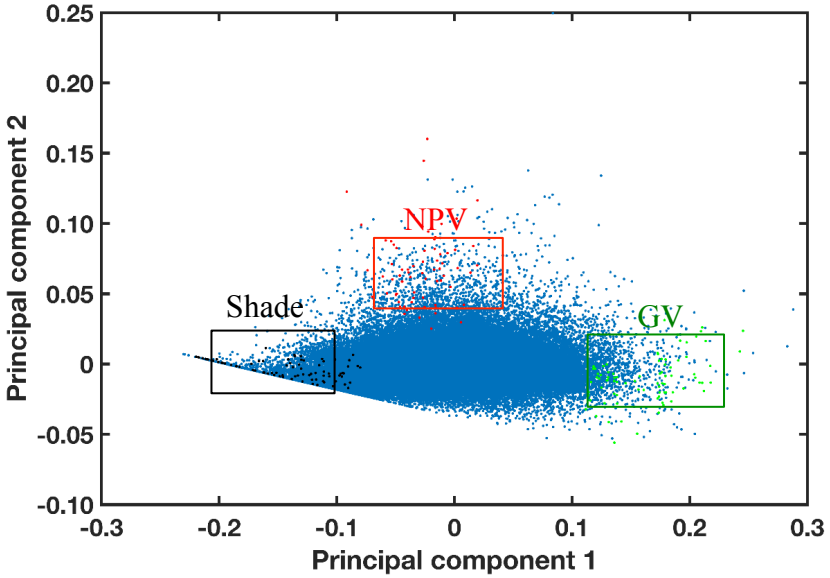

Figure S8. The mean (color lines) and one standard deviation (error bars) of reflectance spectra for three key endmembers derived from the visual assessment (i.e. averaging all the manually identified pure pixels extracted from calibrated PlanetScope images over the dry season of 2018 and 2019 at the k67 site). These three endmembers are pixels of completely leafless tree-crowns for pure non-photosynthetic vegetation (NPV), leafy tree-crowns for pure green vegetation (GV), and deep shade/shadow portions of the canopy (shade).

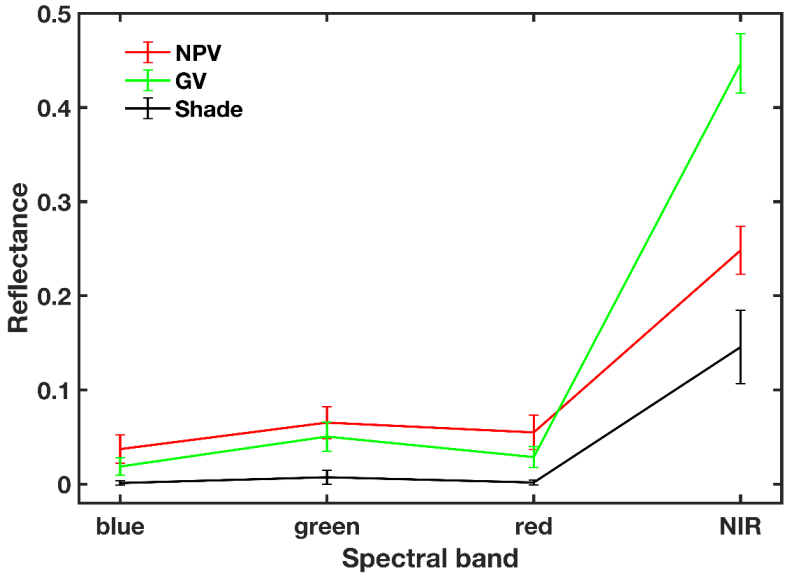

Figure S9. Evaluating the effects of temporal offset and spatial extent on the derived ecosystem-scale seasonal pattern, including the top panel for the temporal analysis and the bottom panel for the spatial analysis. In the top panel, (a) NIR reflectance and (b) EVI of BRDF-adjusted MODIS data is used, and the five time periods (i.e. 2019, 2018, 2010-2011, 2000-2005 and 2000-2019) in a 10km×10km centered on the k67 site are displayed. It is important to note that 2010-2011 and 2000-2005 present the same time periods as that of phenocam and LAI measurements, respectively. Black lines and error bars indicate the mean and one standard deviation of MODIS 20-years mean seasonality. In the bottom panel, (c) NIR reflectance and (d) EVI of the calibrated PlanetScope covering the full dry-season (from June to November) of 2018 is used, and seven spatial extents (i.e. 100m×100m, 200m×300m, 500m×500m, 1km×1km, 3km×3km, 5km×5km, and 10km×10km) centered on the k67 site are displayed. It is important to note that 100m×100m and 200m×300m present the same spatial extents as that of LAI and phenocam measurements, respectively. Black lines and error bars indicate the monthly mean and one standard deviation of the calibrated PlanetScope in the whole 10km×10km area. Light grey shading indicates the dry season of the k67 site.

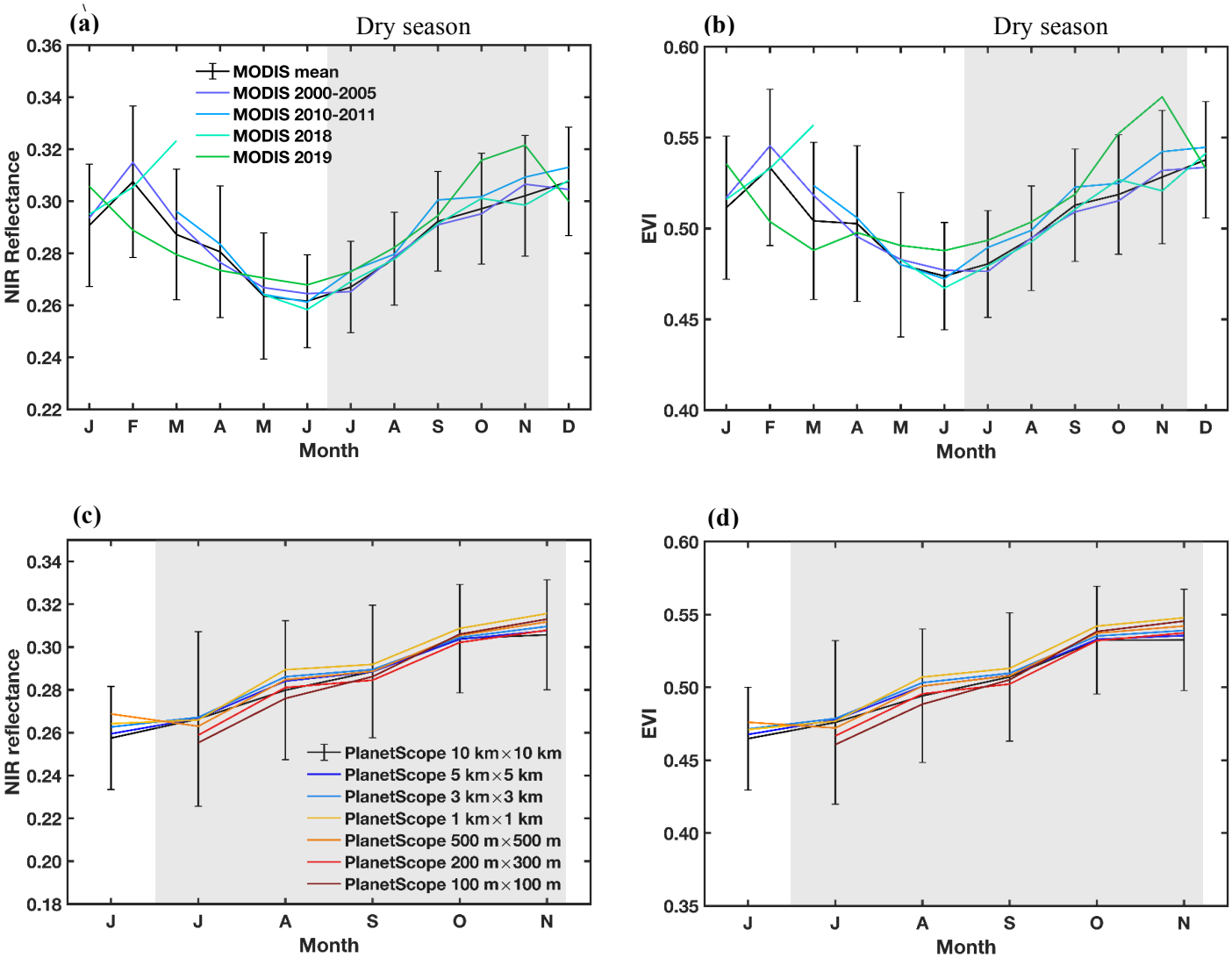

Figure S10. Ecosystem-scale seasonality of BRDF-adjusted MODIS (20-year mean in black and its 95% confidence interval in grey shading, and 2019 gap-filled in red) and 2019 PlanetScope (uncalibrated in blue and calibrated in green), including reflectance bands of (a) blue, (b) green, (c) red, and (d) NIR, and vegetation indices of (e) Normalized Difference Vegetation Index (NDVI), and (f) Enhanced Vegetation Index (EVI). BRDF-adjusted MODIS including both 20-year mean and 2019 gap-filled are displayed as background information; the uncalibrated/calibrated PlanetScope is based on the histogram matching analysis as shown in Fig. 4; and a 3km×3km area centered on the k67 tower site is used to calculate ecosystem-scale seasonality. Light grey shading indicates the dry season of the k67 site.

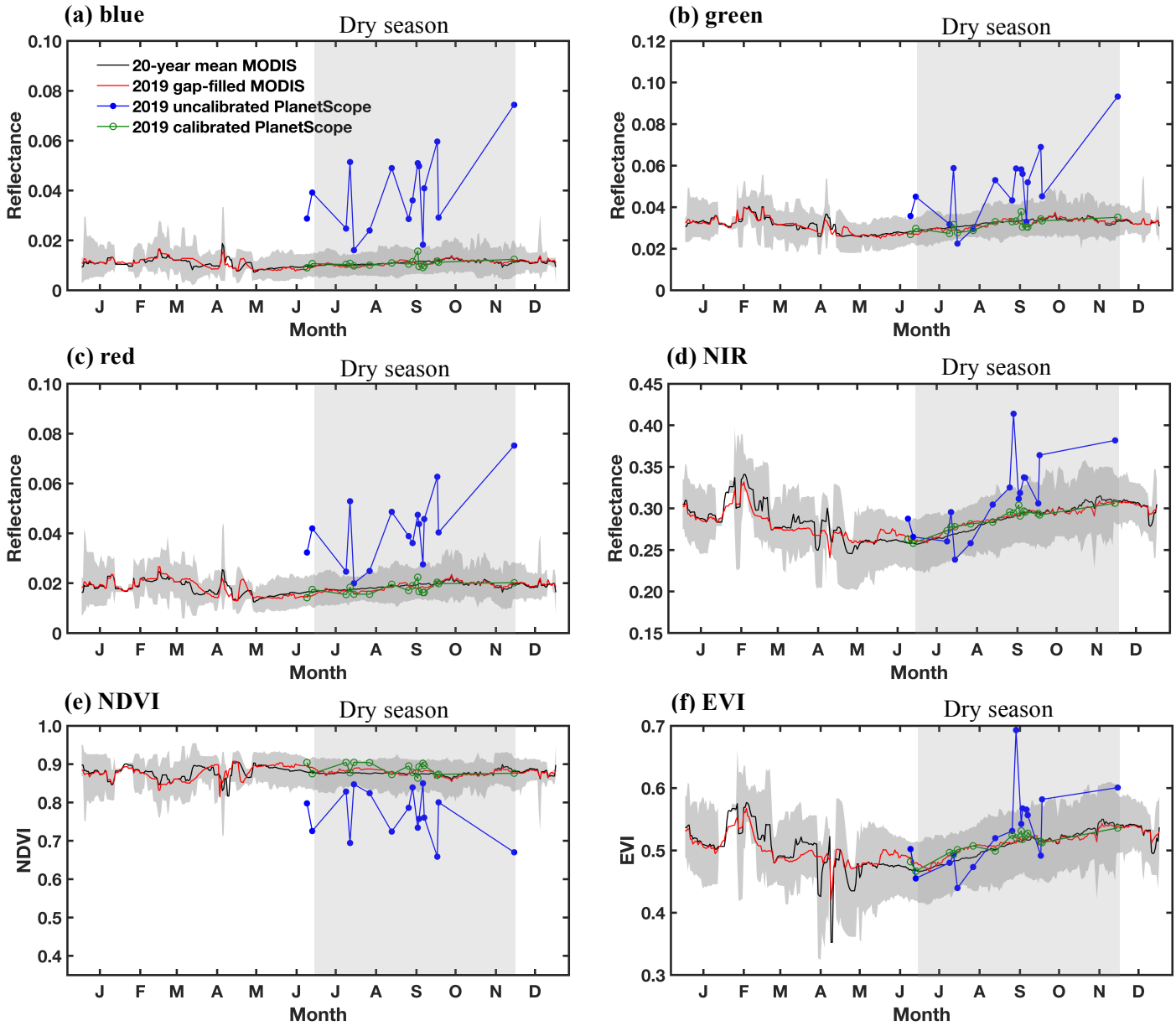

Figure S11. Comparisons of PlanetScope-derived phenology metrics and ground-based phenology measurements, including a) PlanetScope-derived and tower-phenocam measurements of NPV fraction, and b) PlanetScope-derived and tower-phenocam measurements of GV fraction and field LAI measurements. The calibrated PlanetScope data in 2019 are used here, and the PlanetScope-derived phenology metrics represent an average of a 3km×3km area centered on the k67 site; error bars indicate one standard deviation. Tower-phenocam measurements in 2010-2011 (conducted in an about 200m×300m area centered on the k67 site) and field LAI measurements in 2000-2005 (a 100m×100m plot, ~5 km apart from the k67 site) are based on the literature values (Brando et al., 2010; Wu et al., 2016; see methods for details).

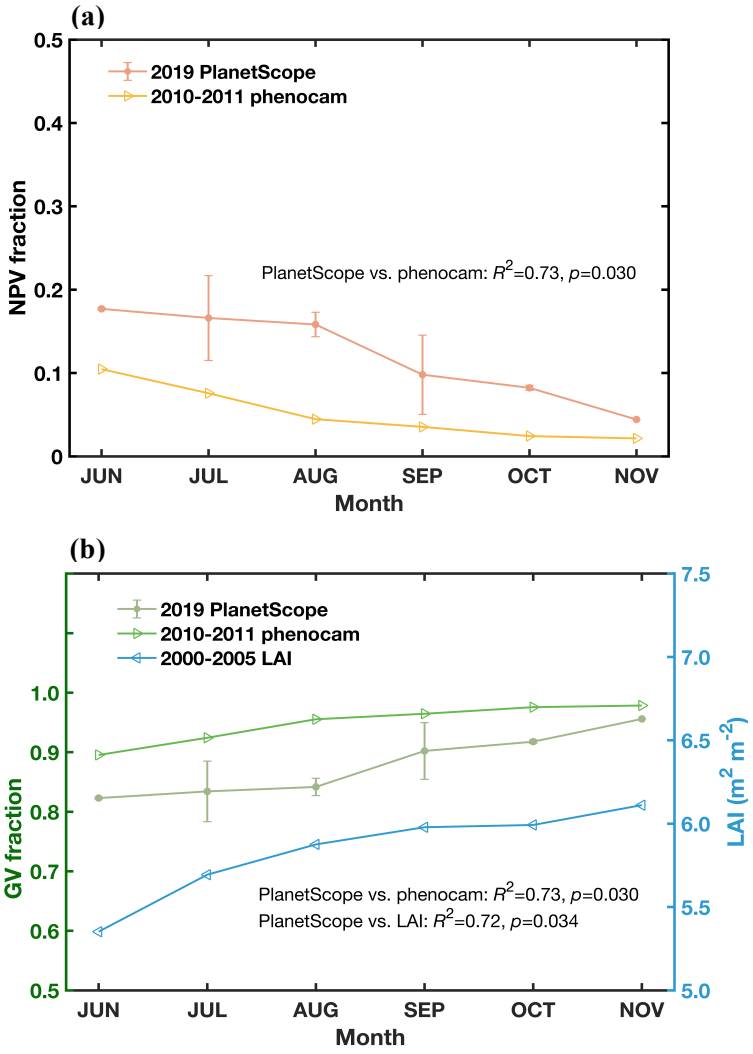

Figure S12. Dry-season trends in NPV fractions derived from two satellites (i.e. PlanetScope and MODIS), plotted against phenocam-derived leafless tree-crown fraction (here also called NPV fraction). PlanetScope of 2018 and BRDF-adjusted MODIS of 2018 and 2010-2011 are all from a 3km×3km area centered on the k67 tower site; NPV fractions derived from the two satellites use the same linear spectral unmixing (including the same endmember-specific reflectance spectra derived from calibrated PlanetScope); error bars indicate one standard deviation. Tower-phenocam-derived leafless tree-crown fraction is available only for 2010-2011 and is adopted from a previous study at the same site (Wu et al., 2016).

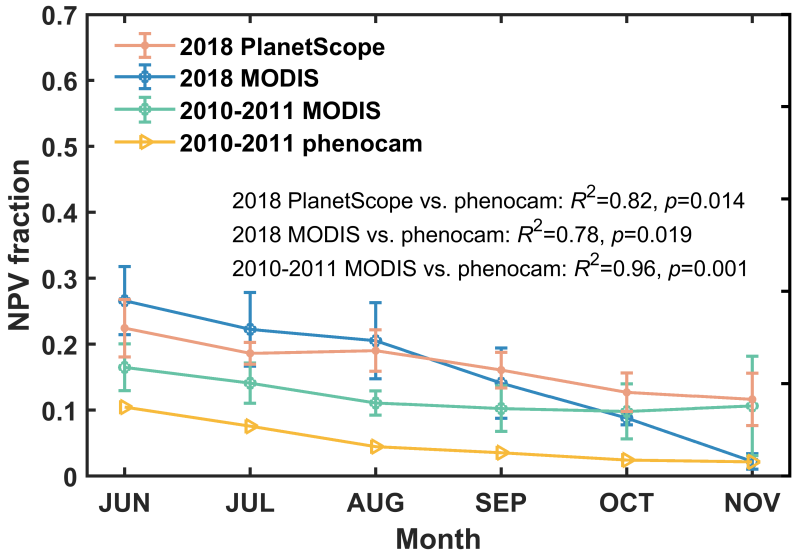

Figure S13. Assessing the dry-season change rate in NPV fraction in a 10km×10km area centered on the k67 tower site, including maps of dry-season change rate in NPV fraction in 2018 (a) and 2019 (b); and statistical summary on frequency distribution of dry-season change rate in NPV fraction in 2018 (c) and 2019 (d). All dates of calibrated PlanetScope in the dry season of 2018/2019 were used to assess the seasonal trend in NPV fraction based on a linear regression analysis. Color bar has a range from -0.005 to 0.005, with a negative value for dry-season decrease in NPV fraction (or green-up) and a positive value rate for dry-season increase in NPV (or brown-down) fraction. The missing values (grey color) indicate those pixels without enough (i.e. n=4) valid day measurements across the full dry-season after applying pixel quality control and cloud/aerosol contaminations removal. The missing values are pronounced in 2019, which might be related with the large-scale Amazon fire in 2019 (Lizundia-Loiola et al., 2020). Overall, our results suggest that the patterns shown in 2018 are comparable with that in 2019.

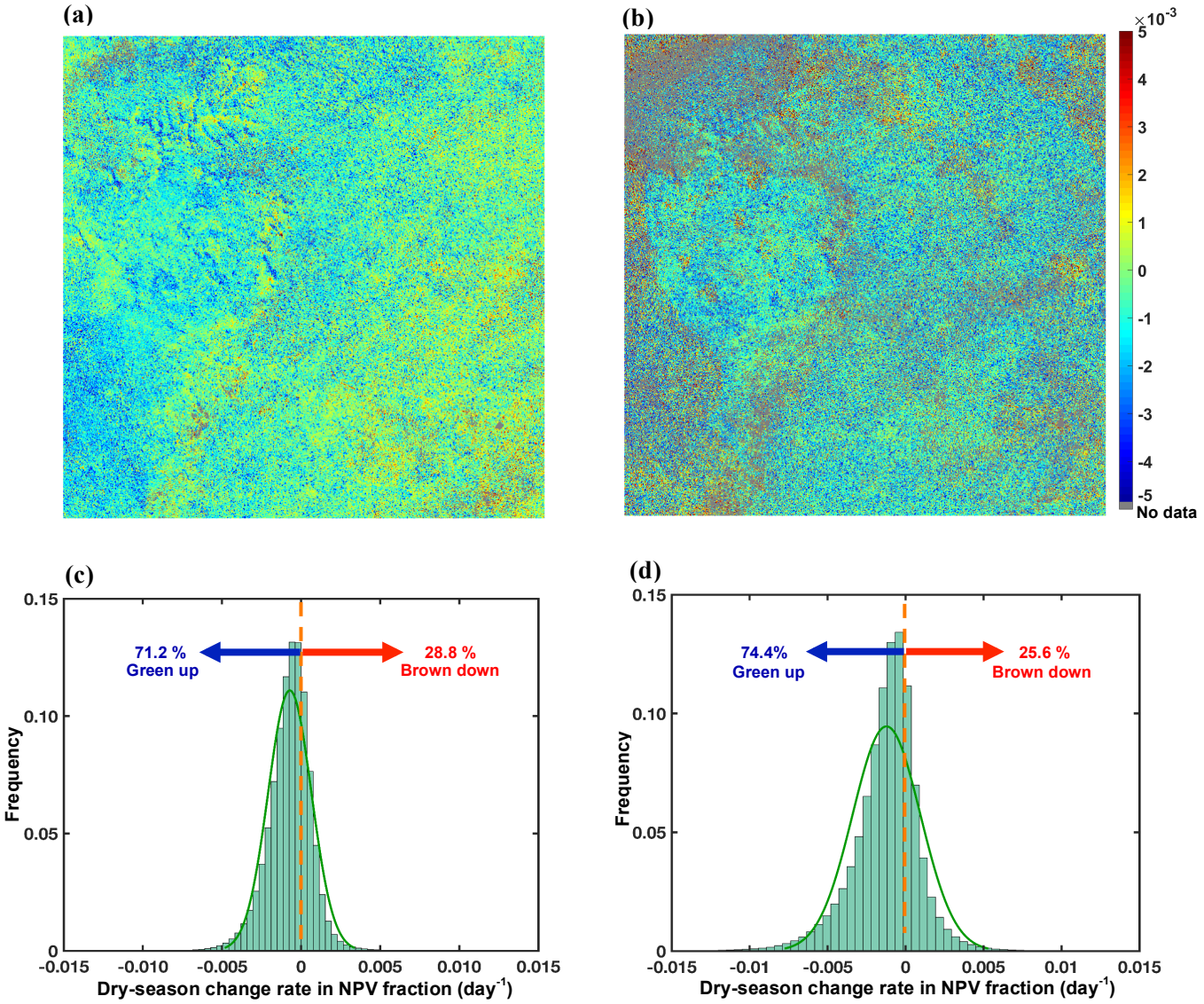

Table 1. Spatial resolutions, accessed data time ranges, and spectral bands and band-specific wavelength ranges of PlanetScope and MODIS data used at the k67 site.

Satellite	Spatial resolution (m)	Accessed data time range	Spectral band and wavelength range (nm)			
			Blue	Green	Red	NIR
PlanetScope	3	06/2018-11/2018 06/2019-11/2019	455-515	500-590	590-670	780-860
MODIS	500	02/2000-12/2019	459-479	545-565	620-670	841-876

References:

Brando, P.M., Goetz, S.J., Baccini, A., Nepstad, D.C., Beck, P.S.A., Christman, M.C., 2010. Seasonal and interannual variability of climate and vegetation indices across the Amazon. Proceedings of the National Academy of Sciences of the United States of America, 107, 14685-14690.

Lizundia-Loiola, J., Pettinari, M. L., & Chuvieco, E., 2020. Temporal Anomalies in Burned Area Trends: Satellite Estimations of the Amazonian 2019 Fire Crisis. Remote Sensing, 12, 151. https://doi.org/10.3390/rs12010151.

Wu, J., Albert, L.P., Lopes, A.P., Restrepo-Coupe, N., Hayek, M., Wiedemann, K.T., Guan, K.Y., Stark, S.C., Christoffersen, B., Prohaska, N., Tavares, J.V., Marostica, S., Kobayashi, H., Ferreira, M.L., Campos, K.S., da Silva, R., Brando, P.M., Dye, D.G., Huxman, T.E., Huete, A.R., Nelson, B.W., Saleska, S.R., 2016. Leaf development and demography explain photosynthetic seasonality in Amazon evergreen forests. Science, 351, 972-976.

Wu, J., Kobayashi, H., Stark, S.C., Meng, R., Guan, K.Y., Tran, N.N., Gao, S.C., Yang, W., Restrepo-Coupe, N., Miura, T., Oliviera, R.C., Rogers, A., Dye, D.G., Nelson, B.W., Serbin, S.P., Huete, A.R., Saleska, S.R., 2018. Biological processes dominate seasonality of remotely sensed canopy greenness in an Amazon evergreen forest. New Phytologist, 217, 1507-1520.